ADVANCED MATERIALS
www.advmat.de

# Peptide-Oligonucleotide Nanohybrids Designed for Precise Gene Therapy of Rheumatoid Arthritis

*Qing Wang, Xiaole Peng, Xiaoting Gao, Yi Qin, Wenhao Li, Zebin Wu, Zhiqi Lao, Ang Gao, Ziyan Mao, Yaozeng Xu, Paul K. Chu, Xin Zhao, Dechun Geng,* and Huaiyu Wang**

**Rheumatoid arthritis (RA) is a chronic autoimmune disease characterized by excessive inflammation, pathological bone resorption, and systemic osteoporosis. It lacks effective treatment due to the complex pathogenesis. Gene therapy, especially targeted oligonucleotide (ON) delivery therapy, offers a new prospect for the precise treatment of RA. Nevertheless, the clinical application of ON delivery therapy still faces various challenges such as the rapid enzymolysis by RNAse, the lack of tissue targeting ability, difficulty in cell membrane penetration, and the incapability of endolysosomal escape. To address these issues, a novel kind of engineered peptide and oligonucleotide (PON) nanohybrids are designed and fabricated, which provide various advantages including good biosafety, inflammatory region-targeted delivery, cell membrane penetration, reactive oxygen species (ROS) scavenging, and endolysosomal escape. The PON nanohybrids produce promising effects in suppressing inflammatory responses and osteoclastogenesis of macrophages via multiple signaling pathways. In vivo administration of PON nanohybrids not only ameliorates local joint bone destruction and systemic osteoporosis in the pathological state, but also demonstrates good prophylactic effects against the rapid progression of RA disease. In conclusion, the study presents a promising strategy for precise RA treatment and broadens the biomedical applications of gene therapy based on delivery system.**

## 1. Introduction

Rheumatoid arthritis (RA) is a chronic autoimmune disorder characterized by excessive inflammation, pathological erosion, progressive loss of joint function, and systemic osteoporosis. As a common and refractory disease, RA afflicts ≈0.5–1.0% of the population worldwide.[1] The etiologies of RA include genetic susceptibility, infections, and autoimmune dysfunctions, but as of now, its pathological mechanism remains unclear.[2] According to the current clinical guidelines, traditional disease-modifying antirheumatic drugs (tDMARDs) such as methotrexate are considered as the first-line therapy of RA. However, the therapeutic effect of tDMARDs is far from satisfaction, which is limited by the slow onset of action, and numerous side effects including hepatotoxicity, renal toxicity, gastrointestinal discomfort, and liver fibrosis.[3] As alternatives to tDMARDs, some novel biologics (infliximab, adalimumab, tocilizumab,

Q. Wang, X. Peng, Y. Qin, W. Li, Z. Wu, Y. Xu, D. Geng
Department of Orthopedics
The First Affiliated Hospital of Soochow University
Suzhou, Jiangsu 215006, China
E-mail: szgengdc@suda.edu.cn

X. Peng
Department of Orthopaedics
The First Affiliated Hospital of Chongqing Medical University
Chongqing 400016, China

X. Gao, Z. Lao, A. Gao, H. Wang
Center for Human Tissues and Organs Degeneration
Shenzhen Institute of Advanced Technology
Chinese Academy of Sciences
Shenzhen 518055, China
E-mail: hy.wang1@siat.ac.cn

The ORCID identification number(s) for the author(s) of this article can be found under https://doi.org/10.1002/adma.202500883

DOI: 10.1002/adma.202500883

Z. Mao
United World College of the Atlantic
St Donat's Castle
Vale of Glamorgan
Llantwit Major CF61 1WF, UK

P. K. Chu
Department of Physics
Department of Materials Science and Engineering
and Department of Biomedical Engineering
City University of Hong Kong
Tat Chee Avenue, Kowloon, Hong Kong, China

X. Zhao
Department of Applied Biology and Chemical Technology
The Hong Kong Polytechnic University
Hung Hom, Hong Kong, China

H. Wang
Key Laboratory of Biomedical Imaging Science and System
Chinese Academy of Sciences
Shenzhen 518055, China

H. Wang
State Key Laboratory of Biomedical Imaging Science and System
Shenzhen 518055, China

 

anakinra, and secukinumab) working by blocking specific receptors to reduce inflammation and immune responses, have been developed for RA therapy.[4] Although these biological drugs can achieve rapid onset of action and inflammation targeting therapy compared to tDMARDs, they still have significant drawbacks, such as immunogenicity-induced drug resistance, increased risk of infections, and rapid relapse after discontinuation.[5] It is undeniable that simply blocking specific receptors cannot thoroughly cure RA, since the onset and progression of RA involve the dysregulation of immune-related genes. Therefore, gene intervention is a potentially viable strategy for RA therapy.

Recent advancements have propelled precision therapies, notably gene therapy, to the forefront of biomedical research. In particular, delivery of oligonucleotides (ONs), such as the intracellular delivery of small interfering RNA (siRNA), messenger RNA (mRNA), and microRNA (miRNA), have aroused great interest.[6,7] These therapeutic agents show excellent biosafety without genetic risks, thus enabling base pairing with targeted RNA to realize gene regulation. In theory, all the diseases related to abnormal gene expressions can be treated by ONs.[8] However, the delivery of ONs to target cells in vivo still provides challenges such as the rapid enzymolysis by RNAse, the lack of tissue targeting ability, difficulty in cell membrane penetration, and the incapability of lysosome escape.[7,9,10] Up to now, a variety of delivery vectors have been developed for addressing these challenges. For instance, viral vectors, especially adenovirus vectors, have shown some success.[11] Nevertheless, these viral vectors pose biosafety concerns as they may cause the host's overactive immune response[12] and even unwanted genomic integration.[13] In comparison, nonviral vectors such as liposomes and cationic polymers are safer, but they still suffer from insufficient payload capacity as well as technical difficulty of further functionalization.[14] Therefore, when using ONs for RA therapy, the primary aim is to develop a safe and effective delivery system which can target specific tissues, penetrate cell membranes, and escape from lysosomal degradation in order to match the complex pathological characteristics of RA and the dynamic delivery process in vivo.

As previously reported, the predilection sites of RA are synovial joints including finger joints, toe joints, wrist joints, etc., of which multiple lesions pose obstacles for local drug delivery.[15,16] Systemic administration, like intravenous administration, is preferable for RA treatment. The ideal ONs delivery system should be capable of long-term circulation in the bloodstream and finally gathering at multiple lesions. Various studies have demonstrated that overactivation of synovial macrophages is noticeable during RA progression. Under such conditions, plenty of synovial macrophages polarize into the pro-inflammatory M1 phenotype, further exacerbating the inflammatory response and activating T cells as antigen-presenting cells.[17] Moreover, the activated macrophages are the precursors of osteoclasts, contributing to joint damage and inflammatory osteoporosis in RA.[18] Therefore, tuning the performance of synovial macrophages is vital to RA treatment. To gain the full advantages of gene therapy, the vectors should facilitate the delivery of ONs to proinflammatory M1 macrophages at synovial joints and enable them to escape timely from the endolysosomal systems afterward. In addition to the regulation of abnormal gene expressions, scavenging excessive reactive oxygen species (ROS) plays a crucial role in RA therapy. This is because the proinflammatory synovial macrophages generate a large amount of ROS at lesion sites, which in turn aggravates the RA condition by amplifying the inflammatory signal pathways.[2,19] In summary, in addition to the above mentioned key points, the ideal ONs delivery systems should also inhibit proinflammatory M1 polarization and osteoclast differentiation, and scavenge ROS to achieve better therapeutic effects in RA treatment.

Herein, we design and fabricate a novel kind of conjugated peptide-oligonucleotide (PON) nanohybrids for RA precise treatment. The PON nanohybrids are readily fabricated by the bioorthogonal click reaction between PEG5-P7-R9-(G-DOPA)4-HPGGPQ-H8-C-DBCO and miRNA-124-A5-($CH_2$)6-Azido (**Scheme 1**). miRNA-124 is chosen as the functional ONs to downregulate the RA-related genes of synovial macrophages, and an amino acid sequence with 9 arginine units (R9) is utilized as the cell-penetrating peptide (CPP) to facilitate the intracellular delivery of miRNA-124. To achieve targeting inflammatory tissues/cells, R9 CPP is capped with polyethylene glycol (PEG5) and 7 proline units (P7) at the N-terminal. In this design, a certain level of ROS at the lesion sites can cleave the P7 linker between PEG5 and R9 and expose the R9 sequence to accomplish cell penetration. At the C-terminal of R9 CPP, 4 repetitive units of 3,4-dihydroxyphenylalanine and flexible glycine ((G-DOPA)4) are added to accentuate the antioxidant effects of nanohybrids.[20] After (G-DOPA)4, the HPGGPQ sequence that can be decomposed by cathepsin K (CTSK) is linked with 8 histidine units (H8) to enable miRNA-124 to detach from the system by enzymolysis and escape timely from the endolysosomal systems via the "proton sponge effect" of H8. Polyadenylate (A5) is added to enhance the stability of miRNA-124,[21] and the FAM group allows fluorescent tracking of miRNA-124 in vivo. The miRNA-124-A5 sequence and the PEG5-P7-R9-(G-DOPA)4-HPGGPQ-H8-C sequence are modified with the azido and dibenzocyclooctane (DBCO) groups respectively, which can be covalently linked by a one-step click reaction to accomplish good specificity and high efficiency. All in all, this engineered delivery system of ONs provides many advantages, including simple synthesis, lesion-targeted delivery, as well as robust capabilities pertaining to cell penetration, ROS scavenging, and endolysosomal escape, revealing a new strategy for RA precise gene therapy.

## 2. Results and Discussion

### 2.1. Synthesis and Characterizations of PEG5-P7-R9-(G-DOPA)4-HPGGPQ-H8-C-DBCO and FAM-miRNA-124-A5-($CH_2$)6-Azido

The PEG5-P7-R9-(G-DOPA)4-HPGGPQ-H8-C-DBCO sequence is constructed by standard Fmoc-mediated solid-phase peptide synthesis.[22] The therapeutic miRNA-124 is modified with A5 at its 3′ end, which is linked to a spacer with 6 $CH_2$ units as well as the terminal azido group. For convenient real-time tracking, the FAM fluorescent motif is added to the 5′ end of miRNA-124-A5-($CH_2$)6-Azido as an option. Based on the bioorthogonal reaction between the DBCO group and the azido group, PEG5-P7-R9-(G-DOPA)4-HPGGPQ-H8-C-DBCO (Peptide-DBCO) and (FAM)-miRNA-124-A5-($CH_2$)6-

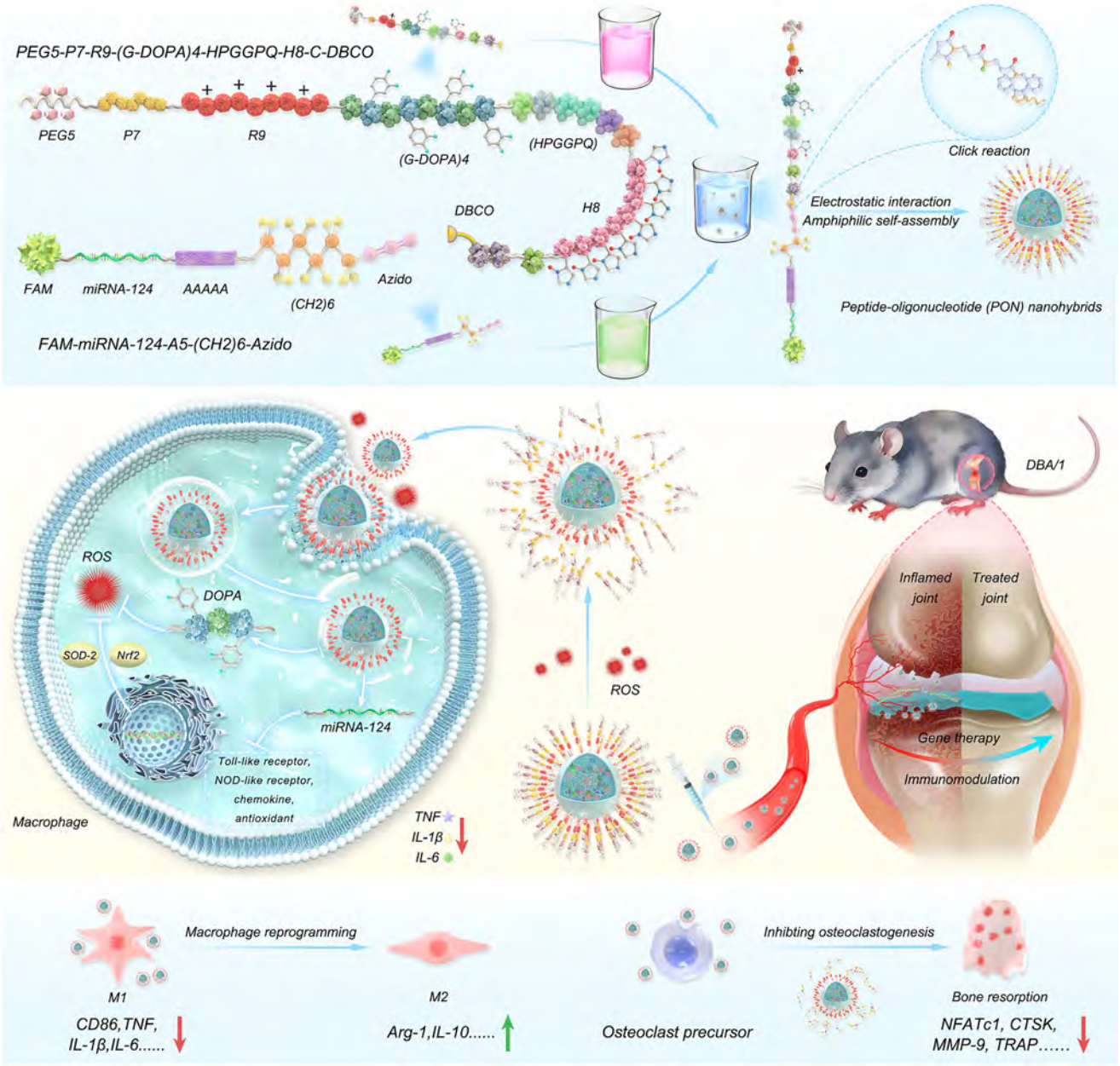


**Scheme 1.** Schematic illustration showing the fabrication and function of PON nanohybrids for RA gene therapy. The PON nanohybrids are readily fabricated by the bioorthogonal click reaction between PEG5-P7-R9-(G-DOPA)4-HPGGPQ-H8-C-DBCO and miRNA-124-A5-$(CH_2)$6-Azido. This system achieves targeted delivery to the lesion sites, robust penetration through cell membrane, efficient scavenging of intracellular ROS, as well as timely escape from the endolysosomes of macrophages, inhibiting proinflammatory M1 polarization and osteoclast differentiation, eventually attenuating arthritic bone destruction and systemic osteoporosis.

Azido ((FAM)-miRNA-124-Azido) is readily coupled to form PON nanohybrids (Scheme 1).

To identify the molecular structures of different sequences, electrospray ionization mass spectrometry (ESI-MS) is performed. As shown in **Figure** 1A,B, the monoisotopic masses $[M-14H]^{14-}$, $[M-13H]^{13-}$, $[M-12H]^{12-}$, $[M-11H]^{11-}$, $[M-10H]^{10-}$, and $[M-9H]^{9-}$ of miRNA-124-Azido/FAM-miRNA-124-Azido are observed at 597.7/636.0, 643.7/685.0, 697.5/742.2, 760.0/809.7, 837.1/890.8, and 930.2/989.8 respectively, which correspond to the theoretical molecular weights of 8380.8/8917.9 Da. The monoisotopic masses $[M+9H]^{9+}$, $[M+8H]^{8+}$, $[M+7H]^{7+}$, $[M+6H]^{6+}$, and $[M+5H]^{5+}$ of Peptide-DBCO are 616.53, 693.85, 792.71, 924.61, and 1110.49 Da, matching the theoretical molecular weight of 5541.10 Da (Figure 1C). Other characteristic peaks can be identified from the $^1$H nuclear magnetic resonance (NMR) spectrum of Peptide-DBCO (Figure 1D,E and Figure S1, Supporting Information). Both ESI-MS and $^1$H NMR confirm the successful synthesis of the various sequences.

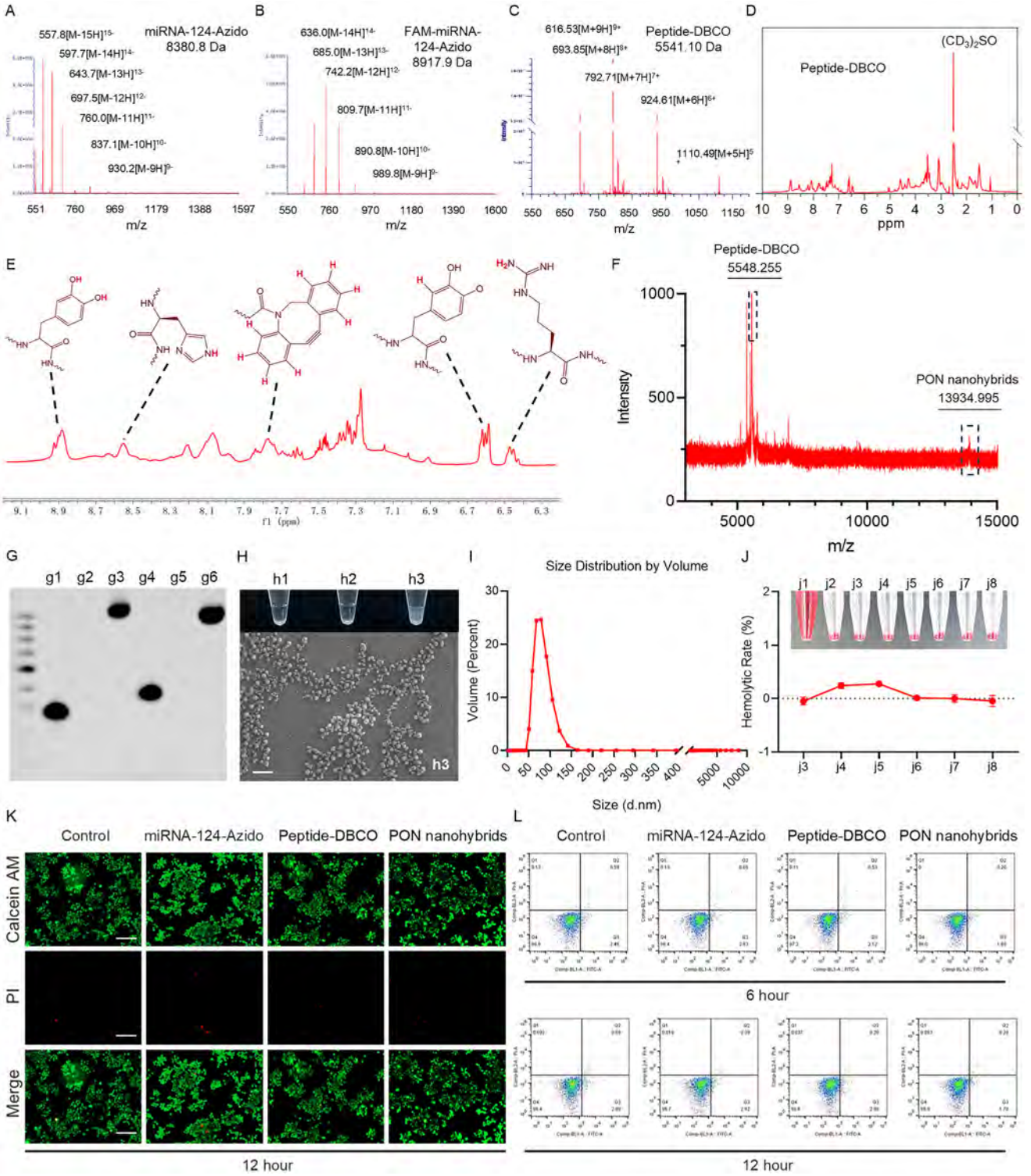


**Figure 1.** Synthesis and characterizations of PON nanohybrids. A–C) ESI-MS analysis of miRNA-124-Azido, FAM-miRNA-124-Azido, and Peptide-DBCO. D,E) $^{1}$H NMR spectrum of Peptide-DBCO and characteristic peaks of different functional groups. F) MALDI-TOF-MS analysis of PON nanohybrids. G) Urea-PAGE analysis of miRNA-124-Azido (g1), Peptide-DBCO (g2 and 5), PON nanohybrids (g3), FAM-miRNA-124-Azido (g4), and FAM-labeled PON nanohybrids (g6). H) Top: Photographs of miRNA-124-Azido (h1), Peptide-DBCO (h2), and PON nanohybrids (h3) in the solution. Bottom: SEM image of the fabricated PON nanohybrids (scale bar = 500 nm). I) DLS measurement of PON nanohybrids. J) Erythrocyte hemolysis assay and quantitative analysis. Positive control (j1), negative control (j2), $500 \times 10^{-9}$ M miRNA-124-Azido (j3), $500 \times 10^{-9}$ M Peptide-DBCO (j4), $200 \times 10^{-9}$ M PON nanohybrids (j5), $500 \times 10^{-9}$ M PON nanohybrids (j6), $1 \times 10^{-6}$ M PON nanohybrids (j7) and $2 \times 10^{-6}$ M PON nanohybrids (j8). K) Live/Dead cell staining (scale bar = 200 μm). L) Flow cytometry analysis of cell apoptosis.

### 2.2. Synthesis and Characterization of PON Nanohybrids

According to our previous studies, the click reaction between the Azido and DBCO groups occurs spontaneously.[23] Therefore, FAM-miRNA-124-Azido/miRNA-124-Azido and Peptide-DBCO are mixed at different ratios to determine the optimal reaction condition. When FAM-miRNA-124-Azido/miRNA-124-Azido and Peptide-DBCO are mixed at a ratio of 2:1, a significant upward shift can be observed from lane a3 and a6 (Figure S2A, Supporting Information), indicating the formation of PON nanohybrids with higher molecular weights. In the meantime, residual RNA bands are observed at the original positions, suggesting that the added FAM-miRNA-124-Azido/miRNA-124-Azido are excessive. By adjusting the feed ratio of FAM-miRNA-124-Azido/miRNA-124-Azido and Peptide-DBCO from 2:1 to 1:1 or 1:2, the reaction of FAM-miRNA-124-Azido/miRNA-124-Azido is complete as no residual RNA bands can be found (Figure 1G and Figure S2B, Supporting Information). Therefore, a reaction ratio of 1:1 is adopted to fabricate PON nanohybrids for the following study.

Matrix-assisted laser desorption/ionization time-of-flight mass spectrometry (MALDI-TOF-MS) is performed to determine the molecular weight of PON nanohybrids. As shown in Figure 1F, the significant peak emerging at 13 934.995 Da after mixing miRNA-124-Azido with Peptide-DBCO corresponds to the theoretical molecular weight of their conjugate. Both the solutions of miRNA-124-Azido (sample h1 of Figure 1H) and Peptide-DBCO (sample h2 of Figure 1H) are transparent, but their mixture is turbid (sample h3 of Figure 1H), suggesting quick self-assembly of PON nanohybrids via electrostatic interactions (Movie S1, Supporting Information). Scanning electron microscopy (SEM) images further confirm the self-assembly of PON nanohybrids (Figure 1H). Dynamic light scattering (DLS) shows that the average size of PON nanohybrids is ≈92.0 nm with a low polydispersity index (PDI) of 0.198 (Figure 1I). The PON nanohybrids are subjected to Urea-PAGE analysis as well as miRNA-124-Azido, NC-RNA (without Azido group), and their mixture with Peptide-DBCO. As shown in Figure S3A (Supporting Information), the bands of miRNA-124-Azido (a1), PON nanohybrids (a3), and NC-RNA (a4) are clearly defined, whereas the mixed group (a6) shows significant tailing, with the band concentrated at the primary NC-RNA position. This is because the covalent bonds formed by click chemistry are more stable than the noncovalent bonds between NC-RNA and Peptide-DBCO. Previous studies have demonstrated that the inflammatory regions in RA are mildly acidic.[24] Our results show that the PON nanohybrids maintain excellent stability in the presence of 10% serum and at different pH (Figure S3B, Supporting Information), fulfilling the stringent requirements of RA therapy.

To evaluate the biosafety of fabricated PON nanohybrids, a series of biological experiments are performed. The hemolysis assay reveals that the hemocompatibility of different concentrations of PON nanohybrids is as good as that of the negative control group (j2) showing a hemolysis rate of less than 1% (Figure 1J). No cytotoxicity can be observed even when the concentration of PON nanohybrids is as high as $5 \times 10^{-6}$ M (Figure S4, Supporting Information). Live/Dead cell staining corroborates that $500 \times 10^{-9}$ M PON nanohybrids are within the biosafety range, as almost all the cells after treatments are alive (Figure 1K). Flow cytometry further demonstrates that the addition of $500 \times 10^{-9}$ M PON nanohybrids does not induce cell apoptosis (Figure 1L). All these characteristics of PON nanohybrids are essential for their practical applications in RA treatment. Considering the biosafety and therapeutic efficacy of PON nanohybrids, the concentration is selected to be $500 \times 10^{-9}$ M for the following in vitro experiments.

### 2.3. Delivery and Endolysosome Escape of PON Nanohybrids

As aforementioned, efficient penetration of cell membrane and rapid escape from endolysosomes into cytoplasm are prerequisites to the intracellular function realization of miRNAs.[9] Furthermore, the target genes should be efficiently delivered to the sites of lesions after administration. To evaluate the biodistribution and inflammatory tissue-targeting properties, the FAM-labeled PON nanohybrids are administered into CIA mice by tail vein injection and monitored by fluorescence imaging. As shown in **Figure** 2A, the FAM fluorescence is rapidly distributed throughout the mice body after injection, with a slow onset of high signal in the limbs after 20 min. The high signal gradually accumulated in multiple joints of mice within 1–12 h. In addition, FAM fluorescence in the bladder increased gradually over 6 h and decreased after urination. Significant high signal was also found in both liver and kidney tissues, especially in kidney, which suggested that the fabricated PON nanohybrids are primarily metabolized by kidneys in vivo.

For inflammatory tissues/cell targeting, a functional sequence of PEG5-P7-R9 is introduced. When the PON nanohybrids are delivered to the lesion sites with abundant inflammatory cells, the PEG5-P7 fragment can be broken by excessive ROS to expose the R9 transmembrane sequence and exert the cell penetration effect.[25] To validate the oxidative cleavage properties of the PEG5-P7 fragment, Peptide-DBCO is subjected to different treatments and then analyzed by liquid chromatography-mass spectrometry (LC-MS). The results show that $H_2O_2$ can reduce the mass of Peptide-DBCO at 37 °C, and the decreased molecular weight roughly corresponds to that of the PEG5-P4 fragment (Figure 2B, Figure S5, Supporting Information). Further addition of vitamin C (a reductive agent capable of neutralizing $H_2O_2$) can terminate the cleavage reaction, corroborating the $H_2O_2$-response of the PEG5-P7 fragment. The cell penetration ability of FAM-labeled PON nanohybrids with or without $H_2O_2$ intervention are evaluated by fluorescence microscopy. As shown in Figure 2C, the intracellular fluorescence of FAM-labeled PON nanohybrids in macrophages are as weak as that of FAM-miRNA-124-Azido. However, after adding $H_2O_2$ to the culture medium, the intracellular FAM fluorescence signal increases significantly with incubation time (Figure 2C and Figure S6, Supporting Information). Flow cytometry confirms that the intracellular FAM fluorescence of the $H_2O_2$ + PON nanohybrids group is higher than that of the other groups (Figure 2D,E). These results validate the ROS-responsive cell penetration characteristics of the delivery system.

In addition to efficient cell penetration, timely lysosome escape is key to effective gene therapy. Therefore, the H8 sequence with "proton sponge effect" is introduced into the PON

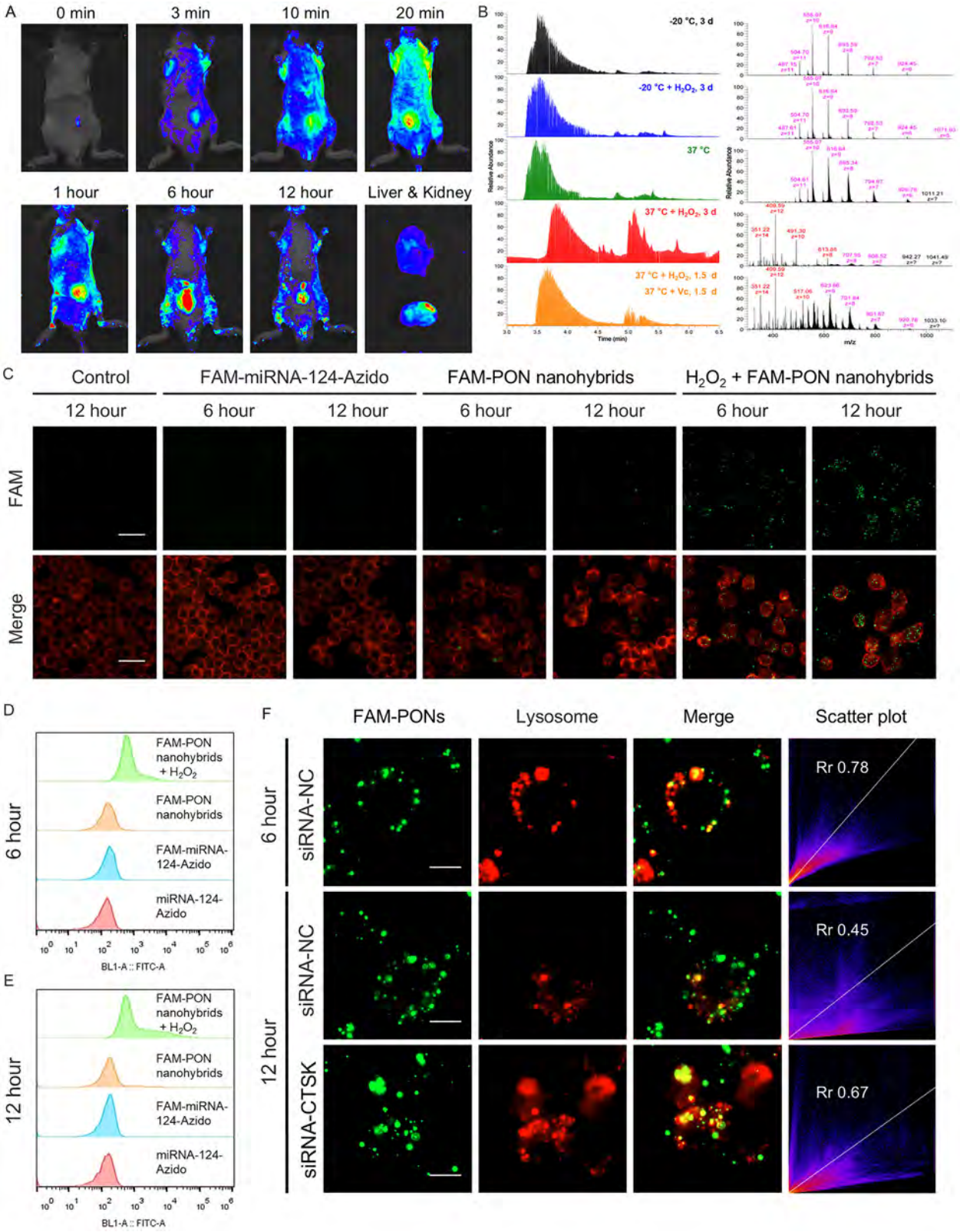


**Figure 2.** ROS-responsive cell penetration and CTSK-mediated endolysosomal escape of PON nanohybrids. A) Whole-body fluorescent imaging analysis of CIA mice after in vivo administration of FAM-labeled PON nanohybrids. B) LC–MS analysis of Peptide-DBCO after different treatments. C) Fluorescence imaging of RAW264.7 cells. FAM-labeled PON nanohybrids are shown in green and the cytoskeleton are stained by Actin-Tracker Red-Rhodamine in red (scale bar = 20 μm). D,E) Flow cytometric analysis of intracellular FAM in RAW264.7 cells. F) Fluorescence colocalization of FAM (green) and commercial lysotracker (red) in RAW264.7 cells (scale bar = 5 μm).

nanohybrids.[26] According to our design, the CTSK in cells can cleave HPGGPQ,[27] and then the exposed H8 sequence enables the escape of targeted genes from endolysosomes into the cytoplasm. As shown in Figure 2F, most of the FAM-labeled PON nanohybrids with green fluorescence overlap the red fluorescence-labeled endolysosomes in the cells after co-incubation for 6 h. When the incubation time is extended to 12 h, there is only a small amount of colocalization between the green and red fluorescence signals, indicating that the majority of PON nanohybrids have escaped from the endolysosomes. To validate our hypothesis, the gene expression of CTSK in the cells is knocked down by siRNA transfection (Figure S7, Supporting Information), and then the PON nanohybrids are added for co-incubation. The results show that rapid lysosome escape of PON nanohybrids is reversed significantly after knocking down the CTSK gene of cells (Figure 2F), indicating the contribution of CTSK to miRNA-124 detaching from PON nanohybrids and further endolysosome escape. Based on the overall ROS-responsive cell penetration and CTSK-mediated lysosome escape, the fabricated PON nanohybrids have great potential for RA gene therapy.

### 2.4. In Vitro Immunoregulatory Properties of PON Nanohybrids

It has been shown that synovial macrophages play a pivotal role in the pathogenesis of RA. As the primary immune defense in joints, synovial macrophages can be broadly classified into pro-inflammatory M1 macrophages and anti-inflammatory M2 macrophages.[17] M1 macrophages are characterized by their secretion of inflammatory cytokines such as TNF-$\alpha$, IL-1$\beta$, and IL-6, and the overexpression of inducible nitric oxide synthase (iNOS) that can produce nitric oxide (NO). NO subsequently reacts with superoxide to form peroxynitrite (ONOO-), which is a potent ROS exacerbating the inflammatory response.[28] In contrast, M2 macrophages can secret anti-inflammatory cytokines such as IL-10 to mitigate excessive inflammation and promote healing. The maintenance of joint homeostasis necessitates a balance between the M1 and M2 macrophages. However, RA pathology is characterized by an overabundance of M1 macrophages and a deficit of M2 macrophages. Consequently, therapeutic strategies should aim at tuning the M1/M2 ratio and reducing ROS production for RA therapy.

To investigate the effects of this delivery system on inflammatory macrophages, the classic in vitro mode is established by utilizing lipopolysaccharide (LPS) to stimulate RAW264.7 cells. The quantitative real-time polymerase chain reaction (qRT-PCR) confirms that LPS stimulation can significantly upregulate the gene expressions of M1 markers of macrophages such as iNOS and CD86, as well as inflammatory cytokines including TNF-$\alpha$ and IL-6. In the meantime, M2 markers such as Arg-1 and CD206 and the anti-inflammatory cytokine IL-10 are downregulated. Unlike miRNA-124-Azido producing very little effect, the PON nanohybrids can reverse the gene expressions of LPS-induced macrophages to the levels of macrophages without LPS intervention (**Figure** 3A–G). Immunofluorescence staining further shows that the treatment involving PON nanohybrids suppresses the iNOS expression of LPS-induced macrophages, while the Arg-1 expression is promoted (Figure 3H–K). Flow cytometry and western blot analysis provide further evidence that the PON nanohybrids can downregulate the expression of CD86 (M1 marker) and upregulate the expression of CD206 (M2 marker); also, the inflammatory cytokines in cells, including IL-6, TNF-$\alpha$, and IL-1$\beta$, are all downregulated (Figure 3L–Q). The enzyme-linked immunosorbent assay (ELISA) shows reduced inflammatory cytokines (TNF-$\alpha$, IL-6) and increased anti-inflammatory cytokine IL-10 in the cell supernatant of PON nanohybrids group (Figure 3R–T). Dihydroethidium (DHE) staining reveals that LPS stimulation increases the intracellular ROS level of macrophages, which can be reversed by the PON nanohybrids but not miRNA-124-Azido (Figure 3U,V). These results corroborate that our delivery system is very effective in alleviating the inflammatory performance of LPS-induced macrophages by modulating the phenotype and scavenging ROS.

### 2.5. Immunoregulatory Mechanism of PON Nanohybrids

The underlying immunoregulatory mechanism of PON nanohybrids is further investigated. High-throughput RNA sequencing (RNA-seq) is performed by using a group of LPS-induced macrophages intervened by PON nanohybrids and those without treatment are used as control. Principal component analysis (PCA) demonstrates a strong correlation and good reproducibility for both treated and control groups (**Figure** 4A). According to the volcano plot results of differentially expressed genes (DEGs), there are 925 upregulated genes and 781 downregulated genes between the treated group and control group (Figure 4B). The upregulated and downregulated DEGs with significant differences are shown together in Figure 4C, and those related to macrophage phenotypes and inflammatory cytokine expressions are highlighted. It is clear that the M1 markers and pro-inflammatory cytokines of LPS-induced macrophages such as TNF, IL18, CD86, and IL6 are downregulated after the treatment of PON nanohybrids. In contrast, the M2 markers and anti-inflammatory cytokines, including Arg1 and Mrc1, are upregulated. Furthermore, the treated group reveals a notable downregulation of osteoclastogenesis-related genes, including Fos, Tnfrsf11a, and Ctsk, as well as the upregulation of Sod2 and Nfe2l2 genes with anti-oxidation effects.

Gene ontology (GO) enrichment is additionally performed to explore the difference in the biological process, cellular component, and molecular function between the treated and control groups. As shown in Figure 4D, immune-related biological processes such as the immune system process, the innate immune response, cellular response to lipopolysaccharide, the inflammatory response, the chemokine-mediated signaling pathway, interleukin-6 production, and chemokine activity (red wireframes), are significantly enriched in the GO analysis. To elucidate the potential signaling pathways, the RNA-seq data are analyzed by Kyoto Encyclopedia of Genes and Genomes (KEGG) enrichment. The results reveal significant enrichment of inflammatory and immune-related signaling pathways such as the Toll-like receptor signaling pathway, as well as downstream pathways such as the NF-$\kappa$B signaling pathway, MAPK signaling pathway, TNF signaling pathway, and chemokine signaling pathway (red wireframes) (Figure 4E). The NOD-like receptor signaling pathway (red wireframe), which can activate the production and release of inflammatory factors through the NLRP3 inflammasome

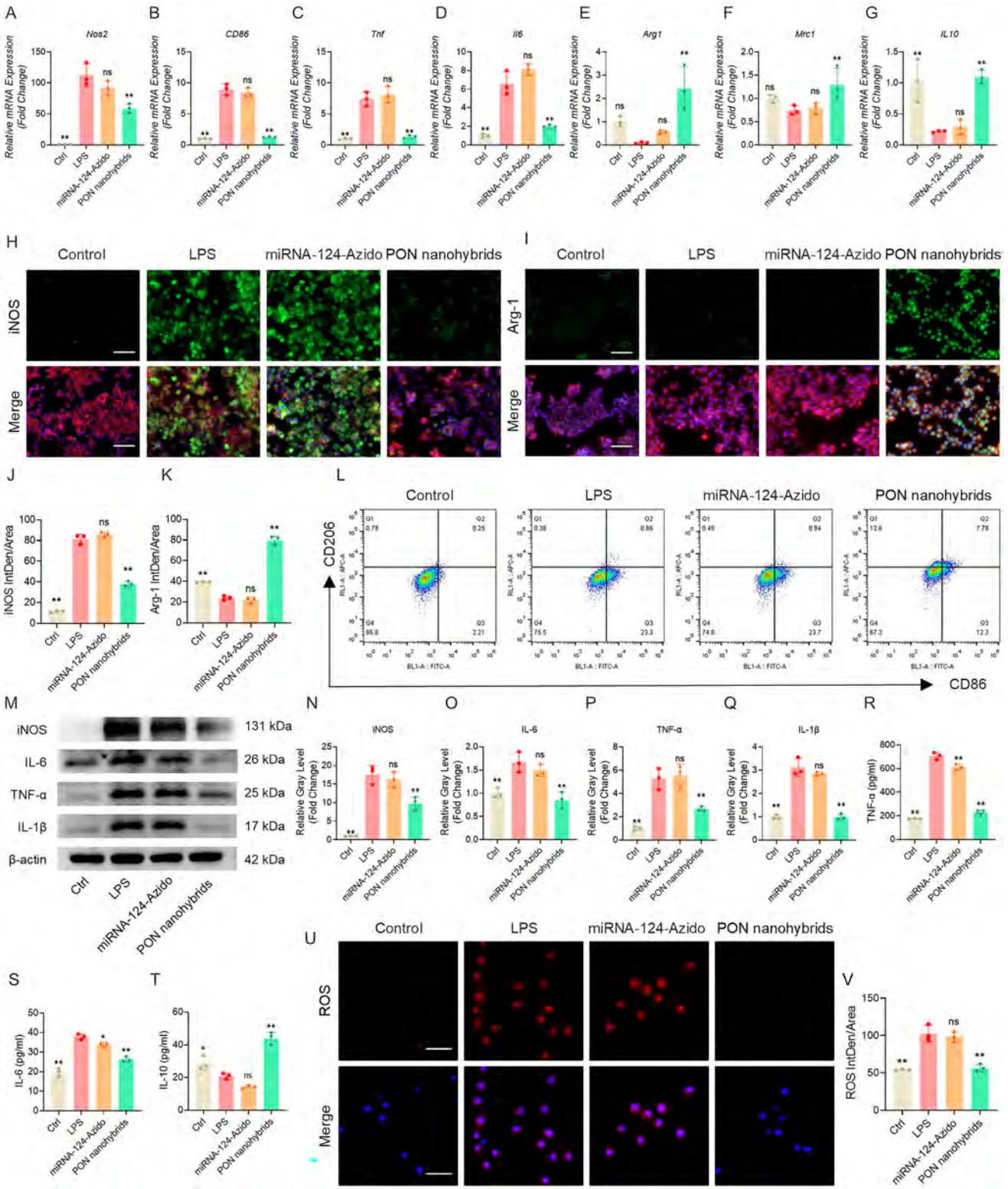


**Figure 3.** Immunoregulatory properties of PON nanohybrids in vitro. A–G) mRNA levels of iNOS, CD86, TNF-$\alpha$, IL-6, Arg-1, CD206 and IL-10 determined by qRT-PCR. H,I) Immunofluorescence staining of iNOS and Arg-1 in green and Red-Rhodamine staining of cytoskeleton in red (scale bar = 200 µm). J,K) Quantitative analysis of iNOS and Arg-1 fluorescence intensity. L) Flow cytometry analysis of membrane markers CD86 and CD206. M–Q) Protein levels of iNOS, IL-6, TNF-$\alpha$, and IL-1$\beta$ determined by western blot analysis. (R-T) ELISA analysis of TNF-$\alpha$, IL-6, and IL-10 in the cell supernatant. U) DHE staining of intracellular ROS (scale bar = 20 µm). V) Quantitative analysis of ROS fluorescence intensity. The miRNA-124-Azido and PON nanohybrids groups represent different treatments under LPS stimulation. $n = 3$ per group, $^{*}p < 0.05$, $^{**}p < 0.01$, and ns: no significance, compared with the LPS group.

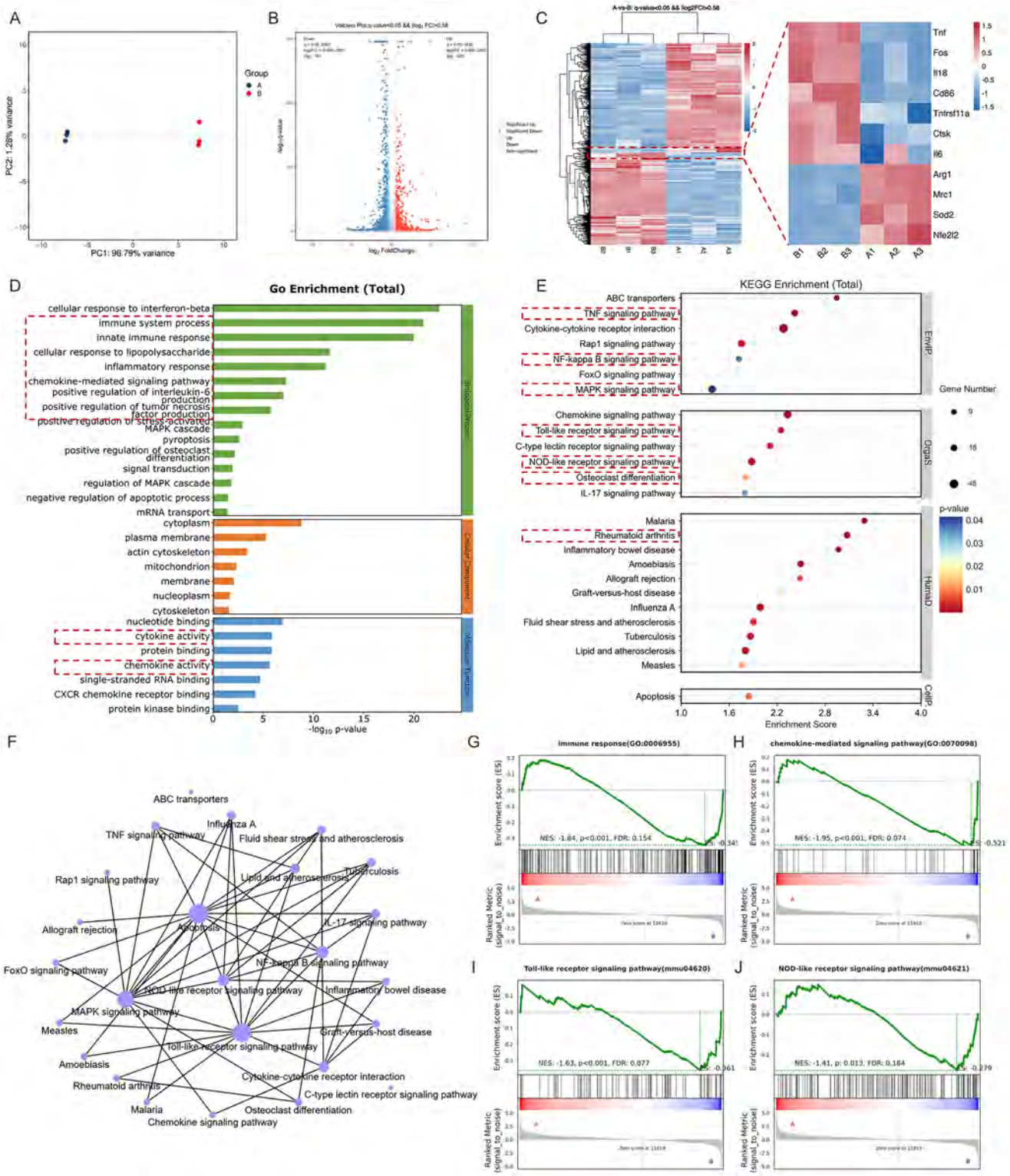


**Figure 4.** Immunoregulatory mechanism of PON nanohybrids A) PCA plot. B) Volcano plot. C) Heat map of total DEGs and those related to macrophage phenotypes and inflammatory cytokines expressions. Group A refers to the cells treated by LPS + PON nanohybrids and group B refers to the cells after LPS intervention. D) GO enrichment analysis of total DEGs. E) KEGG enrichment pathway analysis of total DEGs. F) Correlation network analysis of enriched KEGG pathways. G–J) GSEA analysis of immune response, chemokine-mediated signaling pathway, Toll-like receptor signaling pathway, and NOD-like receptor signaling pathway.

pathway,[29] is also found significantly enriched (Figure 4E). The analysis of the correlation network of the KEGG pathway further indicates the strong interactions in the Toll-like receptor signaling pathway, NF-$\kappa$B signaling pathway, MAPK signaling pathway, TNF signaling pathway, NOD-like receptor signaling pathway, osteoclast differentiation, and rheumatoid arthritis (Figure 4F). GO and KEGG enrichment analysis of all-downregulated DEGs (Figure S8, Supporting Information) and Gene Set Enrichment Analysis (GSEA) further validate that the PON nanohybrids play an important role in the negative regulation of immune response, chemokine-mediated signaling pathway, Toll-like receptor signaling pathway, NOD-like receptor signaling pathway, and other immune related processes. (Figure 4G–J). Additionally, the genes related to RA and other diseases involving macrophage activation[30] such as inflammatory bowel disease, allograft rejection, graft-versus-host disease, lipid and atherosclerosis, and parasitic infection diseases, are all downregulated. These results suggest that the fabricated PON nanohybrids exert desirable immunoregulatory effects by alleviating the inflammatory responses of LPS-induced macrophages via multiple signaling pathways.

### 2.6. In Vitro Anti-Osteoclastogenesis Properties of PON Nanohybrids

Macrophages are the precursor cells of osteoclasts which participate in the bone resorption process of bone remodeling.[31] Since the macrophages are prone to osteoclastic differentiation under inflammatory conditions, the regulatory effect of PON nanohybrids on osteoclastogenesis is additionally evaluated. Briefly, a classical osteoclastogenesis model is established in vitro by subjecting macrophages to RANKL stimulation, followed by different treatments. The results of qRT-PCR show that the osteoclastogenesis-related genes such as NFATc1, CTSK, MMP-9, Acp5, and Atp6v0a3 of the macrophages are significantly upregulated after RANKL stimulation. In contrast, the upregulation of these genes can be reversed by PON nanohybrids but not the miRNA-124-Azido (**Figure** 5A–E), indicating the remarkable anti-osteoclastogenesis of PON nanohybrids. To visualize the osteoclastic differentiation of macrophages after different treatments, tartaric acid phosphatase (TRAP) staining is performed. As shown in Figure 5F, the addition of RANKL induces the formation of abundant TRAP+ multinucleated osteoclasts. The miRNA-124-Azido group shows an insignificant difference from the RANKL group, whereas the size and number of TRAP+ multinucleated osteoclasts decrease significantly after the intervention of PON nanohybrids (Figure 5H,I). The osteoclastic pit formation assay validates that the involvement of PON nanohybrids can reduce the bone resorption area (represented by resorption pits on the bone slice) mediated by mature osteoclasts (Figure 5G,J). The results of western blot are in line with those of qRT-PCR, revealing that the remarkable upregulation of NFATc1, MMP-9, and CTSK proteins in the RANKL group can be restrained by the PON nanohybrids (Figure 5K–N). The RANKL-induced osteoclastic differentiation of macrophages is also accompanied by an increase in intracellular oxidative stress.[32] DHE staining shows that the excessive ROS in the RANKL group is scavenged after the intervention of PON nanohybrids (Figure 5O,P). As shown, the fabricated PON nanohybrids inhibit the RANKL-induced osteoclastic differentiation of macrophages.

### 2.7. Anti-Osteoclastogenesis Mechanism of PON Nanohybrids

RNA-seq analysis is further performed to study the anti-osteoclastogenesis mechanism of PON nanohybrids. In particular, a group of RANKL-induced macrophages are intervened by PON nanohybrids and those without treatment are used as control. There are 352 upregulated genes and 836 downregulated genes between the treated group and the control group (**Figure** 6A), which shows a strong correlation and good reproducibility (Figure 6B). The osteoclastogenesis-related biological processes, including positive regulation of chemokine production, positive regulation of NF-$\kappa$B transcription factor activity, positive regulation of MAPK cascade, negative regulation of osteoclast differentiation, bone resorption, osteoclast differentiation, osteoclast fusion, and the molecular function such as antioxidant activity are significantly enriched in GO analysis (Figure 6C). According to the KEGG results and correlation network analysis, significant enrichment and strong interactions are found from the osteoclastogenesis related signaling such as calcium signaling pathway, Toll-like receptor signaling pathway, chemokine signaling pathway, NOD-like receptor signaling pathway, osteoclast differentiation, rheumatoid arthritis. (Figure 6D,E). Furthermore, rheumatoid arthritis, osteoclast differentiation, mineral absorption, NOD-like receptor signaling pathway, Toll-like receptor signaling pathway, oxidative stress, and redox pathway, oxidative damage response, and chemokine activity are downregulated after the intervention of PON nanohybrids (Figure 6F-M). These results suggest that our delivery system produces desirable anti-osteoclastogenesis effects through multiple signaling pathways.

### 2.8. In Vivo Therapeutic Effects of PON Nanohybrids

We then investigate the therapeutic effects of PON nanohybrids on RA in vivo. To mimic the clinical onset of RA, the classical bovine type II collagen and adjuvant-induced (CIA) mouse model is adopted. In the study, primary and secondary immunization is performed on day 0 and day 21, respectively. Starting on day 22, the experimental mice in different groups are subjected to tail vein injection every 3 days and sacrificed on day 48 (**Figure** 7A). After immunization, the paws of experimental mice are determined by photography, thermographic imaging, and micro-CT scanning to validate the CIA model. The results disclose significant swelling and higher temperature (from ≈26 to ∼34 °C) of the CIA mice's paws on day 48 (Figure S9). Moreover, systemic polyarthritis characterized by joint destruction and osteophyte formation is observed in the forepaws, knees, and hindpaws of the CIA mice (Figure S10, Supporting Information). The RA progression is accompanied by widespread bone loss and decreased bone mass density, leading to osteoporosis in the CIA mice (Figure S11, Supporting Information). The above results have demonstrated successful construction of the CIA model.

After different treatments, the hindpaws of experimental mice are photographed and determined for the thickness. As shown

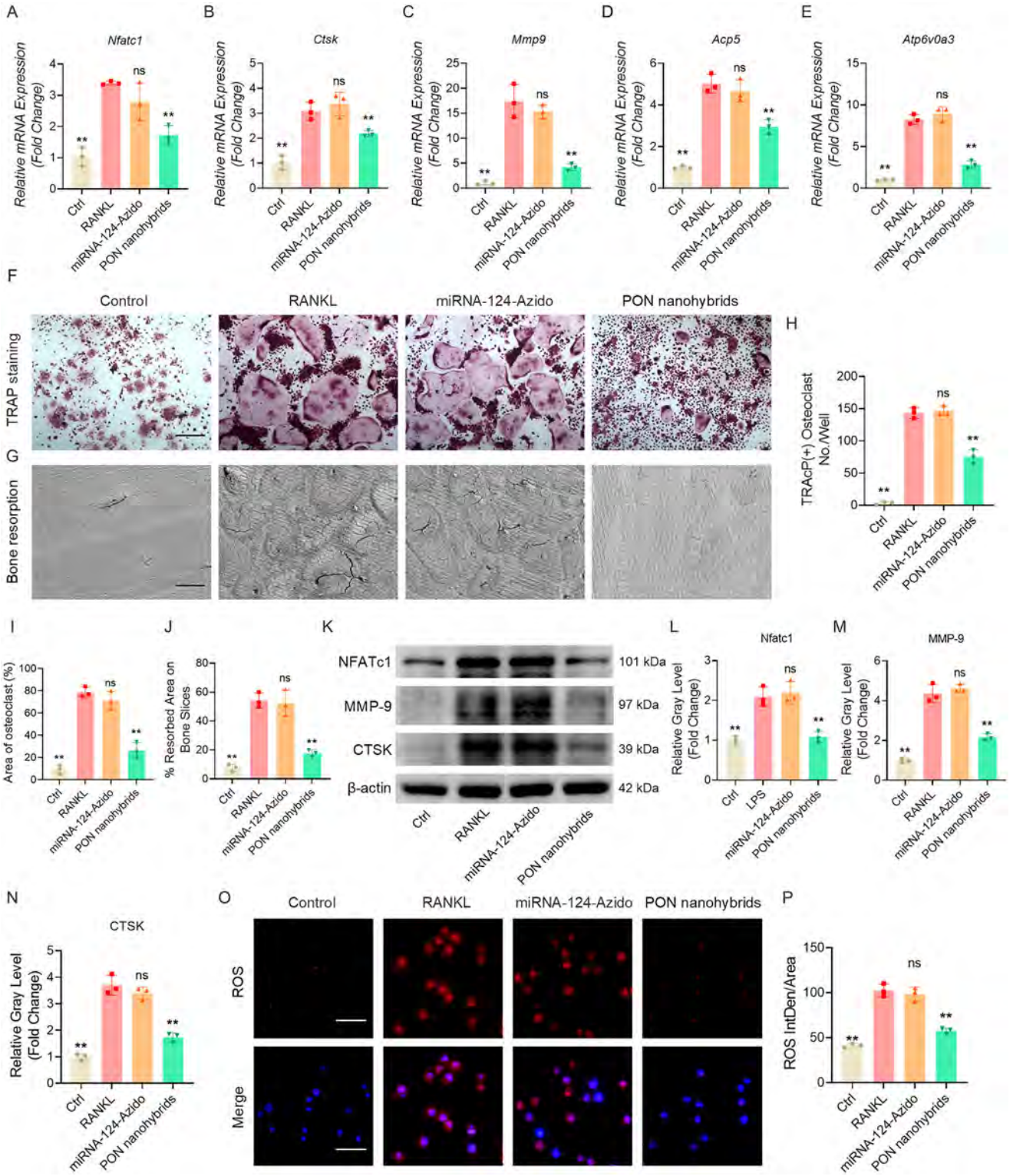


**Figure 5.** Anti-osteoclastogenesis properties of PON nanohybrids in vitro. A–E) mRNA levels of NFATc1, CTSK, MMP-9, Acp5, and Atp6v0a3 determined by qRT-PCR. F) TRAP staining of osteoclasts (scale bar = 100 μm). G) SEM images of bovine bone slices resorption pits (scale bar = 100 μm). H,I) Quantitative analysis of TRAP+ numbers per well and area of osteoclasts. J) Quantitative analysis of resorbed area on bone slices. K–N) Protein levels of NFATc1, MMP-9, and CTSK determined by western blot analysis. O) DHE staining images of intracellular ROS (scale bar = 20 μm). P) Quantitative analysis of ROS fluorescence intensity. The miRNA-124-Azido and PON nanohybrids groups represent different treatments under RANKL stimulation. $n = 3$ per group, $^{*}p < 0.05$, $^{**}p < 0.01$, and ns: no significance, compared with the RANKL group.

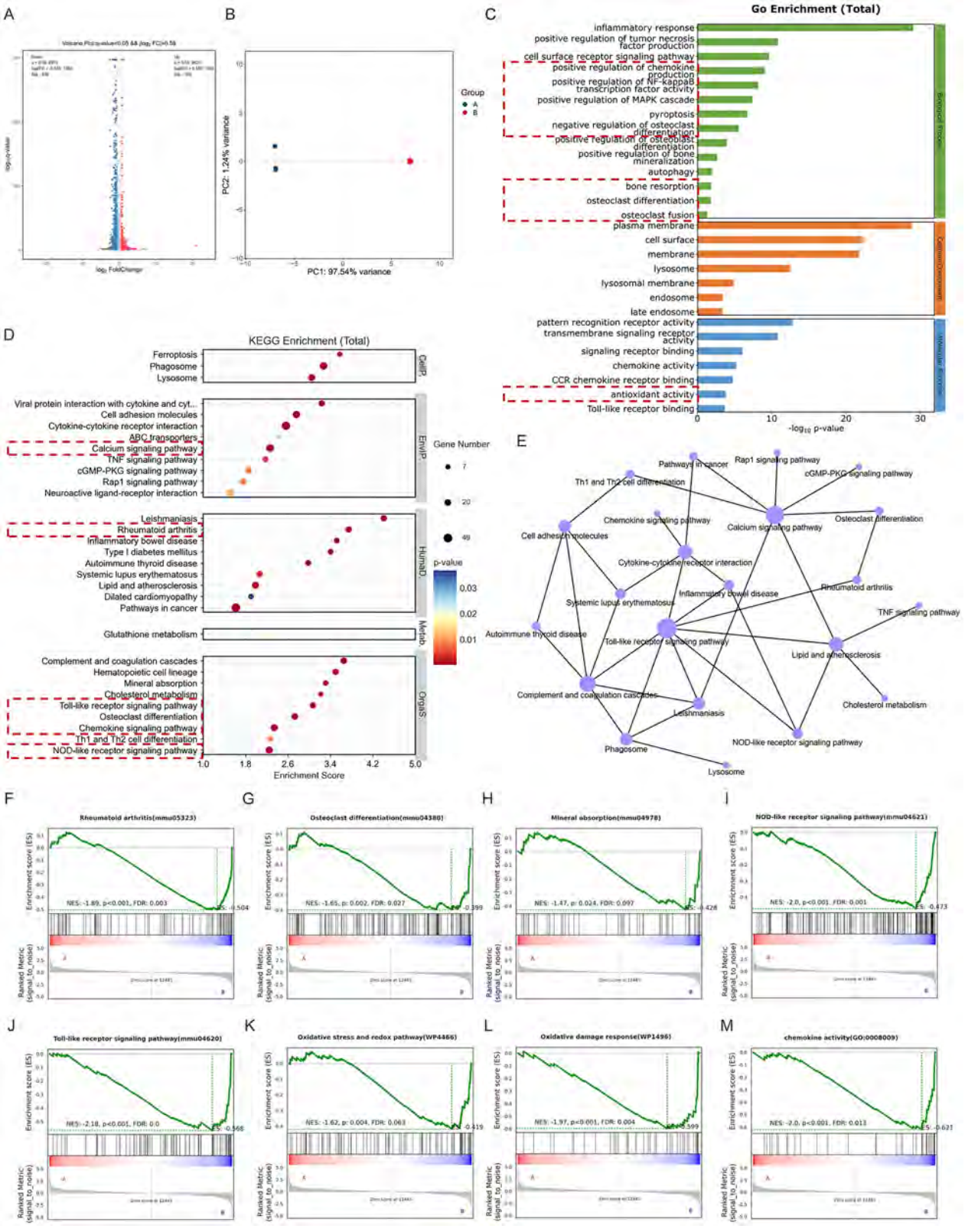


**Figure 6.** Anti-osteoclastogenesis mechanism of PON nanohybrids. A) Volcano plot. B) PCA plot. Group A refers to the cells treated by RANKL + PON nanohybrids and group B refers to the cells after RANKL stimulation. C) GO enrichment analysis of total DEGs. D) KEGG enrichment pathway analysis of total DEGs. E) Correlation network analysis of enriched KEGG pathways. F–M) GSEA analysis of rheumatoid arthritis, osteoclast differentiation, mineral absorption, NOD-like receptor signaling pathway, Toll-like receptor signaling pathway, oxidative stress and redox, oxidative damage response, and chemokine activity pathway.

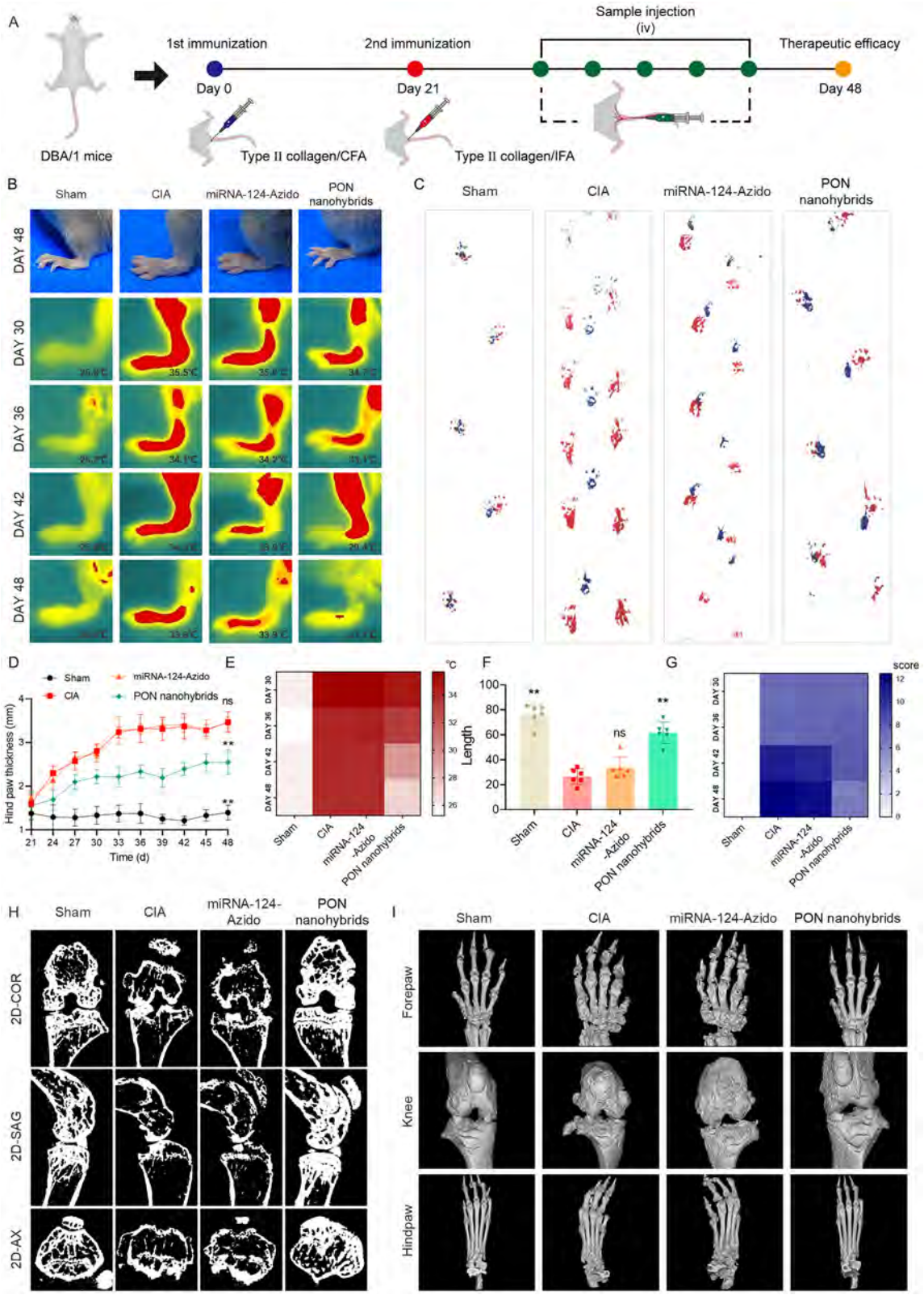


**Figure 7.** Therapeutic effects of PON nanohybrids in vivo. A) Schematic diagram of the experimental protocols. B) Macroscopic observations of hindpaws and thermographic images of hindpaws. C) Representative images of gait analysis. D) Quantitative analysis of hindpaw thickness. E) Heatmap of thermographic images. F) Quantitative analysis of stride length. G) Arthritic score analysis. (H) Two-dimensional micro-CT images of knees. I) 3D micro-CT images of forepaws, knees, and hindpaws. $n = 6$ per group, $^{*}p < 0.05$, $^{**}p < 0.01$, and ns: no significance, compared with the CIA group.

in Figure 7B,D, the intervention of PON nanohybrids alleviates paw swelling of the CIA mice and reduces the hindpaw thickness. The thermographic images reveal that the paw temperature of the mice in the sham group maintains between 25 and 26 °C, whereas that of the CIA group rises to ≈35.5 °C on day 30 and maintains at >33.5 °C until day 48 (Figure 7B,E). Unlike the miRNA-124-Azido with limited effects, the intervention of PON nanohybrids gradually decreases the hindpaw temperature to a normal level (≈27.1 °C) on day 48. The CIA mice treated by PON nanohybrids exhibit a notable improvement in the stride length and reduction of arthritis score, as indicated by the gait analysis (Figure 7C,F) and arthritis score evaluation (Figure 7G). Micro-CT scanning is further performed to evaluate the effects of different treatments on the destroyed multiarticular bone of the CIA mice. In contrast to the significant decrease of trabecular number and discontinuity of joint bone surface shown by the CIA group, treatment with PON nanohybrids increases the joint bone mass of the CIA mice and mitigates the bone erosion and osteophyte formation on the joint bone surface (Figure 7H,I, and Figure S12A, Supporting Information). Bone morphometric analysis confirms that the parameters such as bone mineral density (BMD), bone volume/total volume (BV/TV), bone surface/bone volume (BS/BV), trabecular thickness (Tb. Th), and total porosis (Po tot) of joint bones are improved when the PON nanohybrids are involved (Figure S12B–F, Supporting Information). The systemic bone loss caused by the excessive inflammation of the CIA mice can also be alleviated by this strategy. As shown in Figure S13 (Supporting Information), the treatment using PON nanohybrids increases the number of trabeculae in the lumbar vertebrae and improves the bone morphometric parameters including BMD, BV/TV, BS/BV, Tb. Th, Po tot, trabecular number (Tb. N), and trabecular separation (Tb. Sp). These findings demonstrate that our delivery system can ameliorate the pathological states of the CIA mice.

### 2.9. Histopathological Staining In Vivo

The joints of the hindpaws obtained from different groups are examined by Hematoxylin and Eosin (H&E) staining. Safranin O/Fast Green (F&O) staining is also performed to evaluate cartilage damage, and the activity of osteoclasts in vivo is determined by TRAP staining. As shown in **Figure 8**A, significant synovial hyperplasia, inflammatory cell infiltration, and bone erosion are observed in the knee and ankle joints of the CIA mice. F&O staining and TRAP staining further confirm that in the CIA group, the thickness and integrity of the red-stained articular cartilage are severely disrupted, and the osteoclasts are overactivated in the subchondral bone area. In contrast to the miRNA-124-Azido group with limited therapeutic effects, the treatment using PON nanohybrids ameliorates the pathological symptoms mentioned above. Quantitative analyses of the inflammation area per tissue area (Infl. Ar./T.Ar.), Osteoarthritis Research Society International (OARSI) score, and osteoclast number per tissue area (N.Oc./T.Ar.) verify the effective treatment of polyarthritis using PON nanohybrids (Figure 8B–G).

In the assessment of macrophage infiltration, synovial tissues obtained from different groups are examined by immunofluorescent staining. As shown in Figure 8H, the treatment using PON nanohybrids not only decreases the mass macrophage infiltration of synovial tissues in the CIA mice, but also suppresses the iNOS expression of activated macrophages while promoting the Arg-1 expression. There is a substantial portion of synovial macrophages which tune from the pro-inflammatory state (F4/80+/iNOS+ cells) to the anti-inflammatory state (F4/80+/Arg-1+ cells). DHE staining shows that the synovial ROS level of the CIA mice is significant, which is relieved by PON nanohybrids but not miRNA-124-Azido (Figure S14, Supporting Information). Additionally, the splenic tissues in different groups are examined for the phenotypes of macrophages by flow cytometry. Figure 8I shows that the percentage of M1 macrophages (CD11b+/CD86+ cells) increases from 22.8% of the sham group to 30.5% of the CIA group, and meanwhile, the M2 macrophages (CD11b+/CD206+ cells) decreases from 22% to 16.5%. The involvement of PON nanohybrids reverses the abnormal condition of the CIA mice, with the M1 ratio decreasing to 26.6% and the M2 ratio increasing to 25.3%. ELISA is further performed to examine the levels of serum inflammatory factors after the different treatments. It is shown that the involvement of PON nanohybrids reduces the levels of pro-inflammatory cytokines such as TNF-$\alpha$ and IL-6 in the serum, while upregulating the anti-inflammatory IL-10 cytokine (Figure 8J–L). Finally, the internal organs (heart, liver, lungs, and kidneys) obtained from the experimental mice in different groups are examined by H&E staining (Figure S15, Supporting Information). Negligible damage or inflammation was observed from the main organs of the experimental mice showing the excellent biosafety of PON nanohybrids in vivo.

### 2.10. In Vivo Prophylactic Treatment Using PON Nanohybrids

The above results demonstrate that the PON nanohybrids ameliorates the pathological states of the CIA mice when the symptoms of RA appears. However, it is still unknown whether the PON nanohybrids can produce prophylactic treatment before the onset of RA symptoms. To evaluate the prophylactic effect of PON nanohybrids on RA, different treatments (tail vein injection of experimental mice every 3 days) are conducted between the primary immunization on day 0 and the secondary immunization on day 21.[33] Finally, the experimental mice are sacrificed on day 48 for further assessment (**Figure 9**A).

As shown in Figure 9B,C and Figure S16 (Supporting Information), the pretreatment using PON nanohybrids decreases the swelling, temperature, and thickness of hindpaws after the secondary immunization. In addition to the lower arthritis scores (Figure 9D), the gait abnormalities and stride length of the CIA mice are improved after the pretreatment using PON nanohybrids (Figure S17, Supporting Information). Micro-CT scanning further validates the prophylactic effects of PON nanohybrids on RA, as indicated by the increased bone mass of joint/vertebral bones (Figures S18 and S19, Supporting Information) and the reduced osteophyte formation on multiple joints (Figure 9E). Histological staining, flow cytometry, and ELISA produce consistent results confirming that the PON nanohybrids prevent the onset of RA symptoms (Figure 9F, and Figure S20 and S21, Supporting Information). These findings indicate that our deliver system not only ameliorates the pathological states of the CIA mice but produces excellent prophylactic effects against RA development.

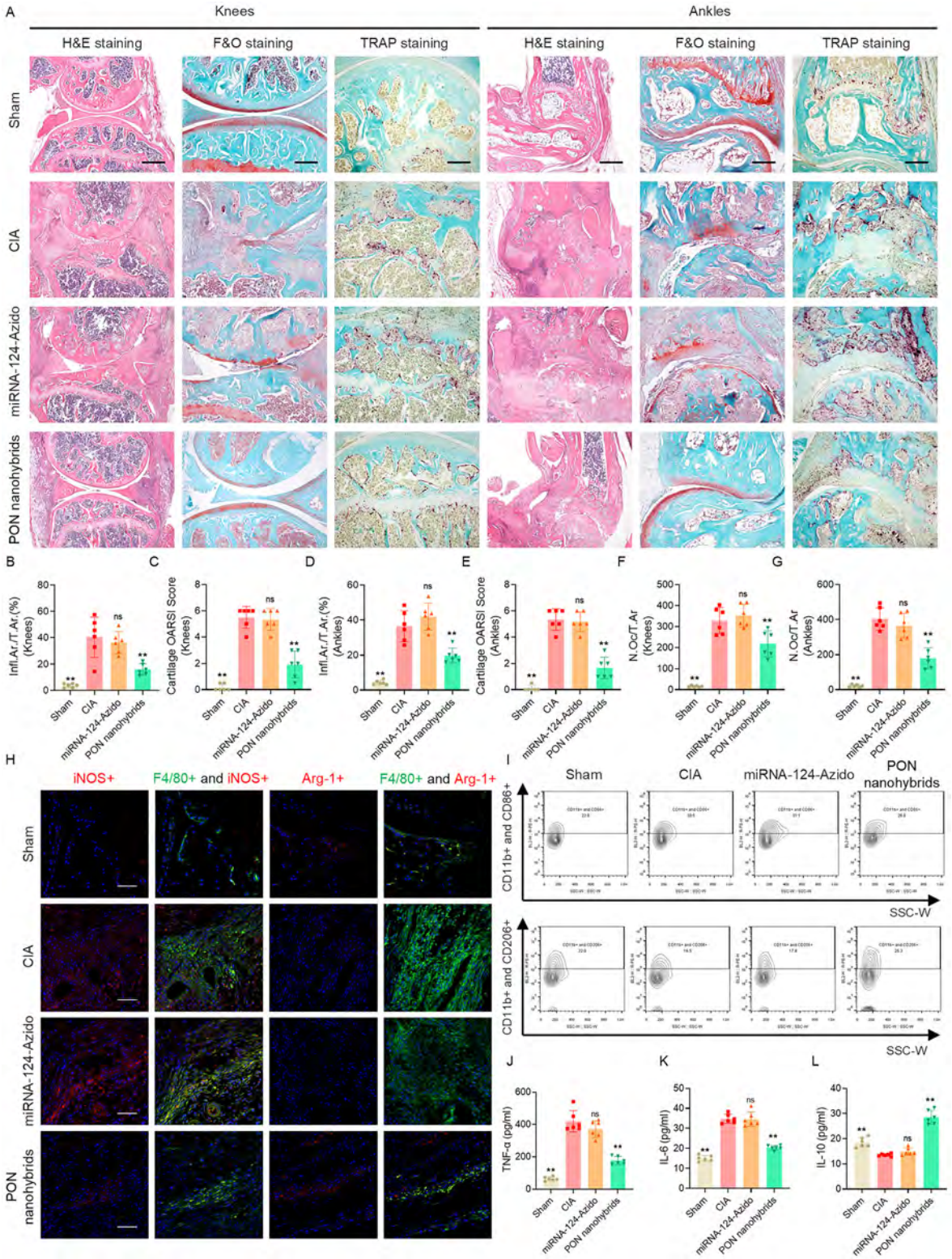


**Figure 8.** Histopathological staining and inflammation assessment in vivo. A) H&E, F&O, and TRAP staining of knees and ankles (scale bar = 800 μm in H&E staining and scale bar = 400 μm in F&O and TRAP staining). B–E) Quantitative analysis of the inflammation area per tissue area (Infl. Ar./T.Ar.) and cartilage OARSI score in knees and ankles. F,G) Quantitative analysis of osteoclast number per tissue area (N.Oc./T.Ar.) in knees and ankles. H) Immunofluorescence staining of F4/80, iNOS, and Arg-1 in knee synovial tissues (scale bar = 200 μm). I) Flow cytometry analysis of CD11b+/CD86+ cells and CD11b+/CD206+ cells in splenic tissues. J–L) ELISA analysis of TNF-$\alpha$, IL-6, and IL-10 in serum. $n = 6$ per group, $^{*}p < 0.05$, $^{**}p < 0.01$, and ns: no significance, compared with the CIA group.

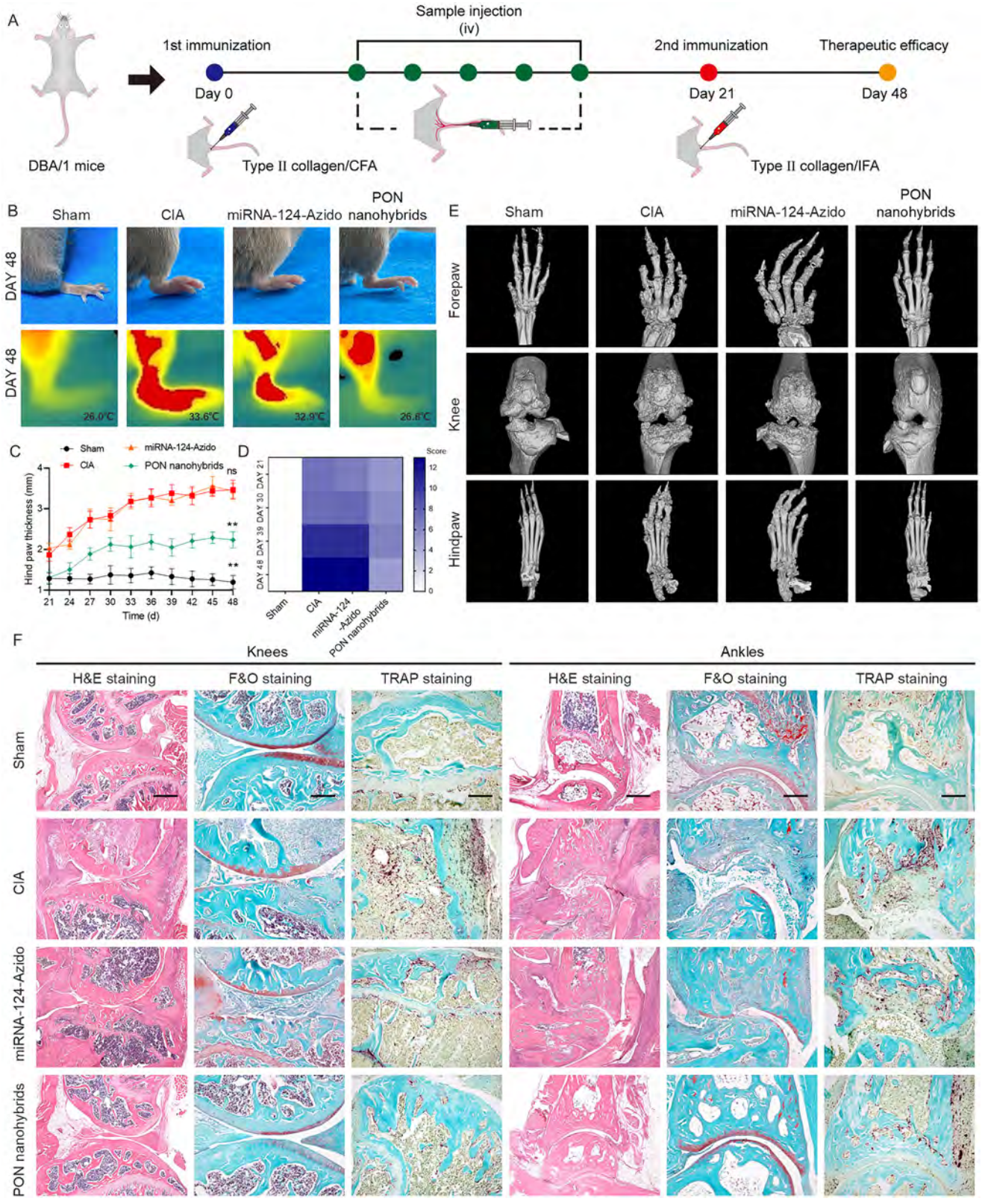


**Figure 9.** Prophylactic effects of PON nanohybrids in vivo. A) Schematic diagram of the experimental protocols. B) Macroscopic observations and thermographic images of hindpaws. C) Quantitative analysis of hindpaws thickness. D) Arthritic score analysis. E) 3D micro-CT images of forepaws, knees, and hindpaws. F) H&E, F&O, and TRAP staining of knees and ankles (scale bar = 800 μm in H&E staining and scale bar = 400 μm in F&O and TRAP staining). $n = 6$ per group, $^{*}p < 0.05$, $^{**}p < 0.01$, and ns: no significance, compared with the CIA group.

Overall, our study proposes a promising strategy for the gene therapy of RA. Nowadays, gene intervention has been widely adopted for the treatment of refractory diseases including RA, and its success mainly depends on the design and development of delivery vectors. In addition to the utilization of cell-penetrating peptide, some other nano-platforms have been developed for RA gene therapy based on metal nanoparticles,[34] metal-organic frameworks[35] and et al,[36] when each provides distinct features of its own. Therefore, our fabricated PON nanohybrids can be rationally integrated with the other delivery vectors to achieve a more advanced strategy for RA gene therapy. It is also worth mentioning that RA is a chronic, systemic autoimmune disease requiring long-term treatment and frequent monitoring. Therefore, compared to the intravenous administration, oral administration is more preferable due to the unparalleled convenience.[37] Toward this goal, we will further refine our delivery system to match the specific requirements of oral route, which can bring new perspectives to RA gene therapy.

## 3. Conclusion

In this study, we design and fabricate a novel kind of engineered PON nanohybrids using a gentle, simple and accurate bioorthogonal strategy. The fabricated PON nanohybrids achieve targeted delivery to lesion sites, robust penetration through cell membrane, efficient scavenging of intracellular ROS, as well as timely escape from the endolysosomal systems of macrophages, downregulating the macrophage inflammatory activation and osteoclastic differentiation. Gene analysis reveals that this is achieved by inhibiting multiple signaling pathways including Toll-like receptor and downstream signaling pathways. In addition, the in vivo administration of PON nanohybrids can not only ameliorate the local joint bone destruction and systemic osteoporosis in a RA mice model, but also provide a good prophylactic effect against the rapid progression of RA disease. Overall, our strategy holds great potential for the treatment of RA. It will also broaden the biomedical applications of oligonucleotide-based gene therapy in many other diseases such as inflammation related diseases dominated by macrophage (e.g., inflammatory bowel disease) or osteolytic diseases dominated by osteoclastic activation (e.g., osteoporosis).

## 4. Experimental Section

*Materials*: Peptide-DBCO (PEG5-PPPPPPP-RRRRRRRRR-G-DOPA-G-DOPA-G-DOPA-G-DOPA-HPGGPQ-HHHHHHHH-C-DBCO) was synthesized by the Fmoc-mediated solid-phase peptide synthesis described in the previous studies.[38] miRNA-124-Azido (miRNA-124-A5-$(CH_2)$6-Azido) and FAM-miRNA-124-Azido (FAM-miRNA-124-A5-$(CH_2)$6-Azido) were provided by Sangon Biotech (Shanghai) Co., Ltd.

*Characterization and Identification*: The molecular weights of different products were determined using a Thermo Scientific LTQ mass spectrometer (ThermoFisher, USA). The DRX500 spectrometer (Bruker, Germany) was used to collect the $^1$H NMR spectra from Peptide-DBCO. LC-MS was performed using a ThermoFisher Exploris 480 (Thermo Fisher, USA) to evaluate the change of Peptide-DBCO after oxidative cleavage.

*Synthesis of PON Nanohybrids*: Peptide-DBCO, miRNA-124-Azido, and FAM-miRNA-124-Azido were separately dissolved in Diethylpyrocarbonate (DEPC) water to a final concentration of $100 \times 10^{-6}$ M and stored at −80 °C. An equal volume of the Peptide-DBCO solution and the miRNA-124-Azido or FAM-miRNA-124-Azido solution was mixed thoroughly at room temperature and stirred for 5 min. (Movie S1, Supporting Information) The molecular weight of PON nanohybrids was determined on the Autoflex Speed MALDI-TOF-MS (Bruker, Germany) and they were stored at −80 °C for further use. The morphology of fabricated PON nanohybrids was observed by SEM (ZEISS, GeminiSEM 300, Germany), and the diameter was determined by DLS (Malvern Zetasizer Nano ZS90, UK).

*Urea-PAGE Analysis*: The urea-PAGE gels were prepared according to the commercial Urea-PAGE Preparation Kit (R0218S, Beyotime, China). An equal amount of different RNA molecules was added to each lane (except for the peptide-only group) and electrophoresed at a constant 120 V RNA ladder. After electrophoresis, the gels were collected and incubated in the Gel Red nucleic acid staining solution (D0139, Beyotime, China) for 30 min and examined by gel imaging (Bio-Rad, USA).

*Hemolysis Assay*: The blood compatibility of different samples was examined by Hemolysis assays with phosphate-buffered saline (PBS) (0% hemolysis) and deionized water (100% hemolysis) as the negative control and positive control, respectively. After different treatments, the red blood cells were centrifuged for 3 min and photographed. Finally, the supernatant was analyzed by measuring the absorbance at 577 nm using a microplate reader, and the hemolysis rate was calculated using the following formula: Hemolysis rate (%) = (absorbance of the experimental group – absorbance of negative control) / (absorbance of positive control – absorbance of negative control) × 100%.

*Cell Culture and Differentiation*: The RAW 264.7 murine macrophages were purchased from the Cell Bank of the Chinese Academy of Sciences (Shanghai, China) and cultured in Dulbecco's Modified Eagle Medium (DMEM, HyClone, USA) supplemented with 10% fetal bovine serum (FBS) at 37 °C. The bone marrow-derived macrophages (BMDMs) were harvested from the femur bone marrow according to our previous studies,[39] and cultured in α-Minimum Essential Medium (α-MEM, HyClone, USA) with 10% FBS and 30 ng/mL macrophage colony-stimulating factor (M-CSF, R&D Systems, USA). As for macrophage M1 polarization, the RAW 264.7 and BMDM cells were induced using 100 ng $mL^{-1}$ LPS (Sigma-Aldrich, USA) for 12 h. As for osteoclast differentiation, the BMDMs were cultured in α-MEM medium containing 30 ng $mL^{-1}$ M-CSF and 50 ng $mL^{-1}$ RANKL (R&D Systems, USA) for 4 days. All the culture media were refreshed every other day.

*Cell Viability Assay*: The cytotoxicity of different products was evaluated by the Cell Counting Kit-8 (CCK-8, C0037, Beyotime, China) assay. Briefly, RAW 264.7 cells were cultured in 96-well plates at a density of 8000 cells/well overnight, and then different concentrations of Peptide-DBCO, miRNA-124-Azido, and PON nanohybrids were added for another 24 h of incubation. Afterward, the cells in different groups were rinsed and incubated with 200 µL of DMEM containing 10 µL of CCK-8 for 1 h at 37 °C in the dark. Finally, the absorbance at 450 nm was determined on a microplate reader. The cell viability was calculated by Cell viability (%) = (absorbance of experimental wells – absorbance of blank wells) / (absorbance of control wells – absorbance of blank wells) × 100%.

*Live/Dead Staining*: Live/dead staining was performed to evaluate the in vitro cytotoxicity of different products. Briefly, RAW264.7 cells were cultured on cell climbing slices in 24-well plates at a density of 30 000 cells/well overnight, and then $500 \times 10^{-9}$ M of Peptide-DBCO, miRNA-124-Azido, and PON nanohybrids were added for another 12 h of incubation. Subsequently, the cells in different groups were incubated with calcein AM (green, $2 \times 10^{-6}$ M) and propidium iodide (red, $4 \times 10^{-6}$ M) according to the manufacturer's instructions for live/dead cell staining kit (AmyJet Scientific, China). The cells after staining were observed under a fluorescence microscope (Zeiss, Germany).

*Flow Cytometry*: Flow cytometry was performed to investigate the cell apoptosis, cell penetration efficiency, and cell phenotype of macrophages after different treatments. As for the assessment of cell apoptosis, Annexin V-FITC and Propidium Iodide (PI) staining were performed following the manufacturer's instructions of Annexin V-FITC Apoptosis Detection Kit (C1062M, Beyotime, China). The levels of Annexin V-FITC and PI were examined to determine the apoptosis levels in different groups. As for the assessment of cell penetration efficiency, miRNA-124-Azido, FAM-miRNA-124-Azido and FAM-labeled PON nanohybrids were used in the

experiments. After different interventions for 6 and 12 h, the cells were harvested and detected at the FAM channel to observe the positive cells. As for the assessment of macrophage polarization in vitro and in vivo, the RAW264.7 cells after different treatments were incubated with PE-CD86 and APC-CD206 antibodies at 1:500 (Biolegend, USA), whereas the splenic cells obtained from experimental mice in different groups were incubated with FITC-CD11b, APC-CD86, and APC-CD206 at 1:500 (Biolegend, USA). Finally, the cells after labeling were analyzed using a FACS Caliber flow cytometer (BD, USA), and quantitative analysis was performed using the FlowJo10 software.

*In Vivo Biodistribution*: The PON nanohybrids was dispersed in PBS and intravenously injected into the tail vein of experimental mice for the evaluation of in vivo distribution. After anesthetizing the mice, depilatory cream was applied to thoroughly remove the fur to avoid the interference of fluorescence imaging. A Lumina Series III in vivo imaging system (Caliper Life Sciences, USA) was used to monitor the bioluminescence at different time points.

*Cell Penetration Analysis*: In addition to flow cytometry analysis, the cell penetration efficiency of different samples was further examined by fluorescence observation. Briefly, RAW264.7 cells were cultured in 24-well plates at a density of 30 000 cells/well overnight, and then refreshed with the medium containing FAM-miRNA-124-Azido, FAM-labeled PON nanohybrids, and $H_2O_2$ + FAM-labeled PON nanohybrids for another 6 and 12 h of incubation. Finally, the cells in different groups were observed under a fluorescence microscope (Zeiss, Germany), and the average fluorescence intensity was measured using the ImageJ software.

*siRNA Transfection*: siRNA-Ctsk was purchased from GenePharma biotech company (China). After culturing the RAW 264.7 cells in 6-well plates at a density of 100 000 cells/well overnight, siRNA-Ctsk transfection was performed according to the manufacturer's instructions of GP-transfect-Mate transfection reagents (GenePharma, China). To verify the gene silencing effect, the mRNA level of Ctsk was detected after 72 h, and the protein level was detected after 96 h.

*Lysosome Escape Analysis*: RAW 264.7 cells were cultured in 24-well plates at a density of 50 000 cells/well overnight with or without siRNA-Ctsk intervention. The FAM-labeled PON nanohybrids ($500 \times 10^{-9}$ M) was added for another 6 and 12 h of incubation. Subsequently, a commercial lysotracker (C1046, Beyotime, China) was added for costaining (60 min at 37 °C) in the dark. Finally, the colocation of FAM and lysotracker in cells was observed under a fluorescence microscope (Zeiss, Germany). The scatter plot analysis was performed using the ImageJ software.

*qRT-PCR Assay*: RAW 264.7 cells were cultured in 6-well plates at a density of 400 000 cells/well overnight. After different treatments, the total RNA of cells was isolated using TRIzol reagent (R0016, Beyotime, China), and the concentration was determined by a NanoDrop 2000 spectrophotometer (Thermo Fisher Scientific). 1 µg of total RNA in different groups was used as the initial template to synthesize complementary DNA (cDNA). After mixing cDNA with SYBR Green PCR Master Mix (Yeasen, Shanghai, China) and corresponding primers, qRT-PCR was performed in a CFX96 thermal cycler (Bio-Rad Laboratories, USA). The primers of target genes were listed in Table S1 (Supporting Information). Relative mRNA expression in different groups was normalized to the average expression of $\beta$-actin and calculated on the basis of the $2^{-\Delta\Delta Cq}$ method.

*Western Blot Analysis*: RAW 264.7 cells were cultured on 6-well plates with a density of 400 000 cells/well overnight. After different treatments, the total proteins of cells were isolated using radioimmunoprecipitation buffer (P0013C, Beyotime, China), and determined for the concentrations using the BCA Protein Assay kit (P0010S, Beyotime, China). Subsequently, ≈20 µg of protein in different groups were electrophoresed on SDS-PAGE (P0012A, Beyotime, China), transferred to nitrocellulose membranes (FFN53, Beyotime, China), and incubated at blocking buffer (P0023B, Beyotime, China) for 1 h. The membranes were incubated with specific primary antibody solutions against $\beta$-Actin (1:1000, Abcam, UK), iNOS (1:1000, Abcam, UK), IL-6 (1:1000, Abcam, UK), TNF-$\alpha$ (1:1000, Abcam, UK), IL-1$\beta$ (1:1000, Abcam, UK), NFATc1 (1:1000, Abcam, UK), MMP-9 (1:1000, Abcam, UK), CTSK (1:1000, Abcam, UK) at 4 °C overnight, and then the corresponding secondary antibody dilutions (1:1000, Abcam, UK) were added for another 1 h of incubation at room temperature. Finally, the membranes were washed by Tris-buffered saline Tween 5 times and incubated with enhanced chemiluminescence reagents (Yeasen, China) for 1 min. The pictures were captured using Image Lab (Bio-Rad Laboratories, USA). The relative grey level of each band was measured by ImageJ software.

*Immunofluorescence Staining and ELISA Analysis*: Initially, RAW264.7 cells were cultured on cell climbing slices on 24-well plates with a density of 30 000 cells/well overnight. After different treatments, the cells in different groups were fixed by 4% paraformaldehyde, permeabilized with 0.2% Triton X-100 (P0096, Beyotime, China), and incubated with the blocking buffer. In the next step, the cells were incubated with specific primary antibody (iNOS, 1:1000, Abcam, UK; Arg-1, 1:1000, Abcam, UK) solutions at 4 °C overnight, and then the corresponding fluorescent secondary antibody (Alexa Fluor488, Abcam, UK) and TRITC-phalloidin (Yeasen, China) were added for another 1 h of incubation at room temperature. Finally, the cells were costained with 4′,6-Diamidino-2′-phenylindole (DAPI, C1002, Beyotime, China) for 10 min and observed under a fluorescence microscope (Zeiss, Germany). The average fluorescence intensity was evaluated using ImageJ software. To further explore the expression levels of various cytokines (IL-6, TNF-$\alpha$, and IL-10), cell culture media were collected from different groups and performed with the ELISA kits (LunChangShuo Biotech, China) according to the manufacturer's instructions.

*ROS Detection*: The RAW264.7 cells were cultured on cell climbing slices in 24-well plates at a density of 30 000 cells/well overnight. After different treatments, the cells were incubated in DHE solution (S0063, Beyotime, China) for 1 h to determine the intracellular ROS levels. Finally, the cells were costained with DAPI (C1002, Beyotime, China) for 10 min and observed under a fluorescence microscope (Zeiss, Germany). The average fluorescence intensity was evaluated using ImageJ software.

*TRAP Staining*: Osteoclasts were obtained from BMDMs as described above. After different treatments, the cells were rinsed with PBS, fixed in a 4% paraformaldehyde solution, and performed with a commercial TRAP Kit (Amizona Scientific, USA) according to the manufacturer's instructions. The fused cells with three or more nuclei were counted as mature osteoclasts. Images were captured by an optical microscope, and quantification was conducted using ImageJ software.

*RNA Sequencing and Differential Gene Expression Analysis*: RAW264.7 cells and BMDMs were cultured in 6-well plates at a density of 300 000 cells/well overnight. After different treatments for 12 h, the total RNA of cells was extracted using the TRIzol reagent (R0016, Beyotime, China). RNA integrity was assessed using the Agilent 2100 Bioanalyzer (Agilent Technologies, USA). The transcriptome sequencing and analysis were conducted by OE Biotech Co., Ltd. (Shanghai, China). The biological duplication of samples was verified by PCA analysis using R (v 3.2.0). DESeq2 was used for the differential gene expression analysis. $Q$ value $< 0.05$ and $|\log2FC| > 0.58$ was set as the threshold for significant differentially expressed genes (DEGs). Based on the hypergeometric distribution, GO, KEGG enrichment analysis, and correlation network analysis of KEGG pathways of DEGs were performed using R (v 3.2.0), and GSEA was performed using the corresponding software.

*Animals*: The male DBA/1 mice (8 to 10 weeks old) were purchased from Shanghai Slaughter Co., Ltd. (China). All animal experiments were authorized by the Ethics Committee of Soochow University (SUDA20240308A03).

*Establish of CIA Model*: The CIA mouse model was established following standardized procedures.[40] Initially, bovine type II collagen (2 mg mL$^{-1}$, CHONDREX, USA) was thoroughly mixed with complete Freund's adjuvant (CHONDREX, USA) at a ratio of 1:1. Next, 0.1 mL of the collagen-adjuvant mixture was injected intradermally at the base of the tail for the first immunization. On day 21, the DBA/1 mice received a second intradermal injection of 0.1 mL of 1:1 mixture of bovine type II collagen (2 mg mL$^{-1}$, CHONDREX, USA) and incomplete Freund's adjuvant (CHONDREX, USA) for booster immunization. The CIA mice were randomly divided into 3 groups, which were administered with the same dose of saline, miRNA-124-Azido, and PON nanohybrids via tail vein injection every 3 days. Starting from day 22, the thermographic analysis of the hindpaws, as well as hindpaw thickness, arthritis scores, and body

weights of different experimental mice, were measured by three independent experimenters.[15,40] On day 48, footprint gait analysis was performed to measure the stride length of experimental mice in different groups. Finally, all groups of mice were sacrificed to collect the serums, spleens, knees, forepaws, hindpaws, and vertebrates for further evaluation.

*Footprint Gait Analysis*: Several sheets of white paper were laid flat on a horizontal table, and a straight passage was created using barriers. The forepaws and hindpaws of the experimental mice from each group were dipped in blue and red ink, respectively. While the mice were in a resting state, they were placed on the track and allowed to move freely. The obtained footprints paper were then scanned, and stride length measurements and analysis were performed using ImageJ software.

*Micro-CT Scanning*: A high-resolution SkyScan1176 micro-CT system (Bruker, Germany) was used to scan the bone tissues of mice in different groups. The scanning procedure was set as 9 µm per layer under 50 kV with a current of 200 µA. 2D/3D reconstruction was performed using the SkyScan1176 software and Mimics Medical software, respectively. The bone morphologic parameters including BMD (g $cm^{-3}$), BV/TV (%), BS/BV(1 $mm^{-1}$), Tb. N (1 $mm^{-1}$), Tb. Th (mm), Po tot (%), and Tb. Sp (mm) were analyzed.

*Histological Staining*: The bone tissues collected from different experimental groups were fixed in 4% paraformaldehyde for a minimum of 48 h, and then decalcified in 10% ethylenediaminetetraacetic acid for 1 month. Following standard dehydration procedures, the specimens were cleared in xylene for 45 min, embedded in paraffin, and sectioned into 6 µm slices using a microtome. After deparaffinization and rehydration, H&E, F&O, and TRAP staining were performed, and the stained sections were examined using a microscope (Carl Zeiss, Germany). Quantitative analysis of inflammation area per tissue area (Infl. Ar./T.Ar.), osteoclast number per tissue area (N.Oc./T.Ar.) was conducted using ImageJ software. Additionally, cartilage damage was assessed using a modified OARSI scoring system,[41] with scored on a scale of 0 (normal), 0.5 (loss of Safranin-O without structural changes), 1 (small fibrillations without loss of cartilage), 2 (vertical clefts down to the layer immediately below the superficial layer and some loss of surface lamina), 3 (vertical clefts/erosion to the calcified cartilage extending to <25% of the articular surface), 4 (extending to 25–50%), 5 (extending to 50–75%) to 6 (extending to >75%).

*Immunofluorescence Staining In Vivo*: The synovial issues collected from different experimental groups were sectioned into 6-µm slices using a frozen microtome. The sections were incubated with Citrate Antigen Retrieval Solution (P0081, Beyotime, China) at 90 °C for 40 min and blocked in Blocking Buffer (P0220, Beyotime, China) for 30 min. Subsequently, the specimens were incubated with specific primary antibody (iNOS, 1:200, Abcam, UK; Arg-1, 1:200, Abcam, UK; F4/80, 1:200, Abcam, UK) solutions at 4 °C overnight, and then the corresponding fluorescent secondary antibody solutions (Alexa Fluor488, Abcam, UK; ABflo594, Abclonal, China) were added for another 1 h of incubation at room temperature. Finally, the sections were costained with DAPI (C1002, Beyotime, China) for 10 min and observed under a fluorescence microscope (Zeiss, Germany).

*ROS Detection In Vivo*: The synovial issues collected from different experimental groups were sectioned into 6 µm slices using a frozen microtome. The sections were incubated in DHE solution (S0063, Beyotime, China) for 1 h to determine the ROS levels in vivo. Subsequently, the specimens were costained with DAPI (C1002, Beyotime, China) for 10 min and observed under a fluorescence microscope (Zeiss, Germany). The average fluorescence intensity was evaluated using ImageJ software.

*ELISA Analysis*: The serums collected from mice in different groups were centrifuged to remove cells and impurities. Afterward, the ELISA kits (LunChangShuo Biotech, China) were used to determine the serum levels of IL-6, TNF-$\alpha$, and IL-10 according to the manufacturer's instructions.

*Statistical Analysis*: Data were presented as mean ± standard deviation. Statistical difference between two groups was analyzed by the student's *t*-test and significant difference between more than two groups was analyzed by the one-way analysis of variance (ANOVA). Statistical significance was defined as $p < 0.05$.

## Supporting Information

Supporting Information is available from the Wiley Online Library or from the author.

## Acknowledgements

Q. W., X. P., X. G. and Y. Q. contributed equally to this work. This work was supported by: National Natural Science Foundation of China (82472525, 82272567, 82272157, 82122002 and 82350710800), Jiangsu Medical Research Project (ZD2022014), Priority Academic Program Development of Jiangsu Higher Education Institutions (PAPD), Program of Suzhou Health Commission (GSWS2022002), National and Local Engineering Laboratory of New Functional Polymer Materials (SDGC2205), Foundation of National Center for Translational Medicine (Shanghai) SHU Branch (SUITM-202403), Project of MOE Key Laboratory of Geriatric Diseases and Immunology (No. KJS2502), City University of Hong Kong Donation Research Grants (DON-RMG 9229021 and 9220061), Collaborative Research Fund, Research Grants Council of Hong Kong (C5044-21G).

## Conflict of Interest

The authors declare no conflict of interest.

## Data Availability Statement

The data that support the findings of this study are available from the corresponding author upon reasonable request.

## Keywords

bioorthogonal click reaction, cell-penetrating peptide, gene therapy, oligonucleotide, rheumatoid arthritis

Received: January 13, 2025
Revised: February 24, 2025
Published online: March 19, 2025

[1] a) I. B. McInnes, G. Schett, *Lancet* **2017**, *389*, 2328; b) J. S. Smolen, D. Aletaha, I. B. McInnes, *Lancet* **2016**, *388*, 2023.
[2] I. B. McInnes, G. Schett, *N. Engl. J. Med.* **2011**, *365*, 2205.
[3] G. P. Aithal, *Nat. Rev. Rheumatol.* **2011**, *7*, 139.
[4] a) P. Emery, M. Buch, *BMJ* **2002**, *324*, 312; b) J. S. Smolen, D. Aletaha, M. Koeller, M. H. Weisman, P. Emery, *Lancet* **2007**, *370*, 1861; c) J. S. Smolen, A. Beaulieu, A. Rubbert-Roth, C. Ramos-Remus, J. Rovensky, E. Alecock, T. Woodworth, R. Alten, O. Investigators, *Lancet* **2008**, *371*, 987.
[5] a) P. A. van Schouwenburg, T. Rispens, G. J. Wolbink, *Nat. Rev. Rheumatol.* **2013**, *9*, 164; b) R. Caporali, F. B. Pallavicini, M. Filippini, R. Gorla, A. Marchesoni, E. G. Favalli, P. Sarzi-Puttini, F. Atzeni, C. Montecucco, *Autoimmun Rev.* **2009**, *8*, 274.
[6] a) Y. Yang, H. Ning, T. Xia, J. Du, W. Sun, J. Fan, X. Peng, *Adv. Mater.* **2023**, *35*, 2301409; b) A. M. Yu, Y. H. Choi, M. J. Tu, *Pharmacol. Rev.* **2020**, *72*, 862; c) X. Peng, Q. Wang, W. Li, G. Ge, J. Peng, Y. Xu, H. Yang, J. Bai, D. Geng, *Bone Res.* **2023**, *11*, 8; d) Q. Wang, W. Wang, X. Peng, G. Ge, W. Li, C. Zhu, X. Chen, S. Guo, N. Li, H. Yang, Y. Xu, J. Bai, G. Pan, D. Geng, *Adv. Funct. Mater. n/a*, 2406503.
[7] T. C. Roberts, R. Langer, M. J. A. Wood, *Nat. Rev. Drug Discov.* **2020**, *19*, 673.

 

[8] M. Metkar, C. S. Pepin, M. J. Moore, *Nat. Rev. Drug Discov.* **2024**, *23*, 67.
[9] R. L. Juliano, *Nucleic Acids Res.* **2016**, *44*, 6518.
[10] W. Wang, Q. Wang, L. Yu, G. Ge, X. Liu, A. Gao, G. Wang, Z. Wu, J. Bai, H. Wang, P. K. Chu, D. Geng, *Biomaterials* **2023**, *302*, 122352.
[11] a) K. A. High, M. G. Roncarolo, *N. Engl. J. Med.* **2019**, *381*, 455; b) K. J. Pasi, S. Rangarajan, N. Mitchell, W. Lester, E. Symington, B. Madan, M. Laffan, C. B. Russell, M. Li, G. F. Pierce, W. Y. Wong, *N. Engl. J. Med.* **2020**, *382*, 29; c) J. R. Mendell, S. Al-Zaidy, R. Shell, W. D. Arnold, L. R. Rodino-Klapac, T. W. Prior, L. Lowes, L. Alfano, K. Berry, K. Church, J. T. Kissel, S. Nagendran, J. L'Italien, D. M. Sproule, C. Wells, J. A. Cardenas, M. D. Heitzer, A. Kaspar, S. Corcoran, L. Braun, S. Likhite, C. Miranda, K. Meyer, K. D. Foust, A. H. M. Burghes, B. K. Kaspar, *N. Engl. J. Med.* **2017**, *377*, 1713.
[12] a) S. J. Aronson, P. Veron, F. Collaud, A. Hubert, V. Delahais, G. Honnet, R. J. de Knegt, N. Junge, U. Baumann, A. Di Giorgio, L. D'Antiga, V. M. Ginocchio, N. Brunetti-Pierri, P. Labrune, U. Beuers, P. J. Bosma, F. Mingozzi, *Hum. Gene Ther.* **2019**, *30*, 1297; b) T. E. Bryson, C. M. Anglin, P. H. Bridges, R. N. Cottle, *Yale J. Biol. Med.* **2017**, *90*, 553.
[13] G. N. Nguyen, J. K. Everett, S. Kafle, A. M. Roche, H. E. Raymond, J. Leiby, C. Wood, C. A. Assenmacher, E. P. Merricks, C. T. Long, H. H. Kazazian, T. C. Nichols, F. D. Bushman, D. E. Sabatino, *Nat. Biotechnol.* **2021**, *39*, 47.
[14] H. Yin, R. L. Kanasty, A. A. Eltoukhy, A. J. Vegas, J. R. Dorkin, D. G. Anderson, *Nat. Rev. Genet.* **2014**, *15*, 541.
[15] M. Zhu, B. Yu, J. Bai, X. Wang, X. Guo, Y. Liu, J. Lin, S. Hu, W. Zhang, Y. Tao, C. Hu, H. Yang, Y. Xu, D. Geng, *J. Bone Miner. Res.* **2019**, *34*, 739.
[16] G. Ge, J. Bai, Q. Wang, X. Liang, H. Tao, H. Chen, M. Wei, J. Niu, H. Yang, Y. Xu, Y. Hao, Y. Xue, D. Geng, *Sci. China Life Sci.* **2022**, *65*, 588.
[17] a) M. Kurowska-Stolarska, S. Alivernini, *Nat. Rev. Rheumatol.* **2022**, *18*, 384; b) I. A. Udalova, A. Mantovani, M. Feldmann, *Nat. Rev. Rheumatol.* **2016**, *12*, 472.
[18] a) N. Komatsu, H. Takayanagi, *Nat. Rev. Rheumatol.* **2022**, *18*, 415; b) G. Schett, E. Gravallese, *Nat. Rev. Rheumatol.* **2012**, *8*, 656.
[19] U. Fearon, M. Canavan, M. Biniecka, D. J. Veale, *Nat. Rev. Rheumatol.* **2016**, *12*, 385.
[20] C. Zhao, J. Chen, J. Ye, Z. Li, L. Su, J. Wang, Y. Zhang, J. Chen, H. Yang, J. Shi, J. Song, *Angew. Chem., Int. Ed. Engl.* **2021**, *60*, 14458.
[21] S. F. Torabi, A. T. Vaidya, K. T. Tycowski, S. J. DeGregorio, J. Wang, M. D. Shu, T. A. Steitz, J. A. Steitz, *Science* **2021**, 371.
[22] L. Liu, X. Tian, Y. Ma, Y. Duan, X. Zhao, G. Pan, *Angew. Chem., Int. Ed. Engl.* **2018**, *57*, 7878.
[23] a) Z. Yang, X. Zhao, R. Hao, Q. Tu, X. Tian, Y. Xiao, K. Xiong, M. Wang, Y. Feng, N. Huang, G. Pan, *Proc. Natl. Acad. Sci. USA* **2020**, *117*, 16127; b) G. Ge, W. Wang, Q. Wang, M. Wang, T. Wang, L. Yu, X. Zhang, C. Zhu, Y. Xu, H. Yang, J. Bai, G. Pan, D. Geng, *Adv. Funct. Mater.* **2024**, 34; c) Z. Du, F. Qiao, L. Tong, W. Zhang, X. Mou, X. Zhao, M. F. Maitz, H. Wang, N. Huang, Z. Yang, *Innovation* **2024**, *5*, 100671; d) X. Chen, X. Li, W. He, M. Wang, A. Gao, L. Tong, S. Guo, H. Wang, G. Pan, *Innovation* **2023**, *4*, 100483.
[24] I. Goldie, A. Nachemson, *Acta Orthop. Scand.* **1970**, *41*, 354.
[25] a) S. H. Lee, T. C. Boire, J. B. Lee, M. K. Gupta, A. L. Zachman, R. Rath, H. J. Sung, *J. Mater. Chem. B* **2014**, *2*, 7109; b) S. S. Yu, R. L. Koblin, A. L. Zachman, D. S. Perrien, L. H. Hofmeister, T. D. Giorgio, H. J. Sung, *Biomacromolecules* **2011**, *12*, 4357; c) C. Y. Sun, S. Shen, C. F. Xu, H. J. Li, Y. Liu, Z. T. Cao, X. Z. Yang, J. X. Xia, J. Wang, *J. Am. Chem. Soc.* **2015**, *137*, 15217.
[26] Y. Zhao, H. Jiang, J. Yu, L. Wang, J. Du, *Angew. Chem. Int., Ed. Engl.* **2023**, *62*, 202304692.
[27] a) F. Lecaille, E. Weidauer, M. A. Juliano, D. Bromme, G. Lalmanach, *Biochem. J.* **2003**, *375*, 307; b) F. A. Jaffer, D. E. Kim, L. Quinti, C. H. Tung, E. Aikawa, A. N. Pande, R. H. Kohler, G. P. Shi, P. Libby, R. Weissleder, *Circulation* **2007**, *115*, 2292.
[28] a) W. Jing, C. Liu, C. Su, L. Liu, P. Chen, X. Li, X. Zhang, B. Yuan, H. Wang, X. Du, *Front. Immunol.* **2023**, *14*, 1107670; b) E. Naik, V. M. Dixit, *J. Exp. Med.* **2011**, *208*, 417; c) Y. Xu, Y. Li, A. Gao, P. K. Chu, H. Wang, *Innovation Life* **2023**, *1*, 100015.
[29] a) Z. Shen, S. Kuang, Y. Zhang, J. Chen, S. Wang, C. Xu, Y. Huang, M. Zhang, S. Huang, J. Wang, C. Zhao, Z. Lin, X. Shi, B. Cheng, *Innovation* **2024**, *5*, 100547; b) P. K. Anand, R. K. Malireddi, J. R. Lukens, P. Vogel, J. Bertin, M. Lamkanfi, T. D. Kanneganti, *Nature* **2012**, *488*, 389; c) B. R. Sharma, T. D. Kanneganti, *Nat. Immunol.* **2021**, *22*, 550.
[30] a) A. Sica, A. Mantovani, *J. Clin. Invest.* **2012**, *122*, 787; b) G. J. Koelwyn, E. M. Corr, E. Erbay, K. J. Moore, *Nat. Immunol.* **2018**, *19*, 526; c) L. M. Hegarty, G. R. Jones, C. C. Bain, *Nat. Rev. Gastroenterol. Hepatol.* **2023**, *20*, 538.
[31] a) N. Takegahara, H. Kim, Y. Choi, *Exp. Mol. Med.* **2024**, *56*, 264; b) L. Tong, A. J. V. Wijnen, H. Wang, D. Chen, *The Innovation Life* **2024**.
[32] H. Kanzaki, F. Shinohara, I. Kanako, Y. Yamaguchi, S. Fukaya, Y. Miyamoto, S. Wada, Y. Nakamura, *Redox Biol.* **2016**, *8*, 186.
[33] G. Shi, Y. Zhou, W. Liu, C. Chen, Y. Wei, X. Yan, L. Wu, W. Wang, L. Sun, T. Zhang, *Acta Pharm. Sin. B* **2023**, *13*, 2778.
[34] Y. Yang, L. Guo, Z. Wang, P. Liu, X. Liu, J. Ding, W. Zhou, *Biomaterials* **2021**, *264*, 120390.
[35] a) L. Guo, Y. Chen, T. Wang, Y. Yuan, Y. Yang, X. Luo, S. Hu, J. Ding, W. Zhou, *J. Control. Release* **2021**, *330*, 119; b) L. Guo, S. Zhong, P. Liu, M. Guo, J. Ding, W. Zhou, *Small* **2022**, *18*, 2202604.
[36] a) J. Chen, J. Tan, J. Li, W. Cheng, L. Ke, A. Wang, Q. Wang, S. Lin, G. Li, B. Wang, J. Chen, P. Zhang, *Small Methods* **2023**, *7*, 2300678; b) H. Han, J. Xing, W. Chen, J. Jia, Q. Li, *Nat. Commun.* **2023**, *14*, 944.
[37] a) L. Zhang, H. Peng, W. Zhang, Y. Li, L. Liu, T. Leng, *Theranostics* **2020**, *10*, 8479; b) N. Hu, L. Zhu, L. Zhang, J. Wang, Y. Wang, J. Luo, L. He, Z. Hao, L. Zhang, *Mater. Today Biol.* **2022**, *16*, 100384.
[38] a) J. Bai, G. Ge, Q. Wang, W. Li, K. Zheng, Y. Xu, H. Yang, G. Pan, D. Geng, *Research* **2022**, *2022*, 9823784; b) M. Li, J. Bai, H. Tao, L. Hao, W. Yin, X. Ren, A. Gao, N. Li, M. Wang, S. Fang, Y. Xu, L. Chen, H. Yang, H. Wang, G. Pan, D. Geng, *Bioact. Mater.* **2022**, *8*, 309.
[39] C. Yang, H. Tao, H. Zhang, Y. Xia, J. Bai, G. Ge, W. Li, W. Zhang, L. Xiao, Y. Xu, Z. Wang, Y. Gu, H. Yang, Y. Liu, D. Geng, *Autophagy* **2022**, *18*, 2817.
[40] D. D. Brand, K. A. Latham, E. F. Rosloniec, *Nat. Protoc.* **2007**, *2*, 1269.
[41] S. S. Glasson, M. G. Chambers, W. B. Van Den Berg, C. B. Little, *Osteoarthritis Cartilage* **2010**, *18*, S17.

 

# Supporting Information

## Peptide-Oligonucleotide Nanohybrids Designed for Precise Gene Therapy of Rheumatoid Arthritis

*Qing Wang, Xiaole Peng, Xiaoting Gao, Yi Qin, Wenhao Li, Zebin Wu, Zhiqi Lao, Ang Gao, Ziyan Mao, Yaozeng Xu, Paul K. Chu, Xin Zhao, Dechun Geng, * Huaiyu Wang **

Qing Wang, Xiaole Peng and Xiaoting Gao, Yi Qin contributed equally to this work

Qing Wang, Xiaole Peng, Yi Qin, Wenhao Li, Zebin Wu, Yaozeng Xu and Dechun Geng
Department of Orthopedics, The First Affiliated Hospital of Soochow University, Suzhou 215006, Jiangsu, China.
E-mail: szgengdc@suda.edu.cn (Dechun Geng)

Xiaoting Gao, Zhiqi Lao, Ang Gao and Huaiyu Wang
Center for Human Tissues and Organs Degeneration, Shenzhen Institute of Advanced Technology, Chinese Academy of Sciences, Shenzhen 518055, China.
E-mail: hy.wang1@siat.ac.cn (Huaiyu Wang)

Xiaole Peng
Department of Orthopaedics, The First Affiliated Hospital of Chongqing Medical University, Chongqing 400016, China.

Ziyan Mao
United World College of the Atlantic, St Donat's Castle, Llantwit Major, Vale of Glamorgan, CF61 1WF, United Kingdom.

Paul K. Chu

Department of Physics, Department of Materials Science and Engineering, and Department of Biomedical Engineering, City University of Hong Kong, Tat Chee Avenue, Kowloon, Hong Kong, China.

Xin Zhao
Department of Applied Biology and Chemical Technology, The Hong Kong Polytechnic University, Hung Hom, Hong Kong

Huaiyu Wang
Key Laboratory of Biomedical Imaging Science and System, Chinese Academy of Sciences, Shenzhen 518055, China.

Huaiyu Wang
State Key Laboratory of Biomedical Imaging Science and System, Shenzhen 518055, China.

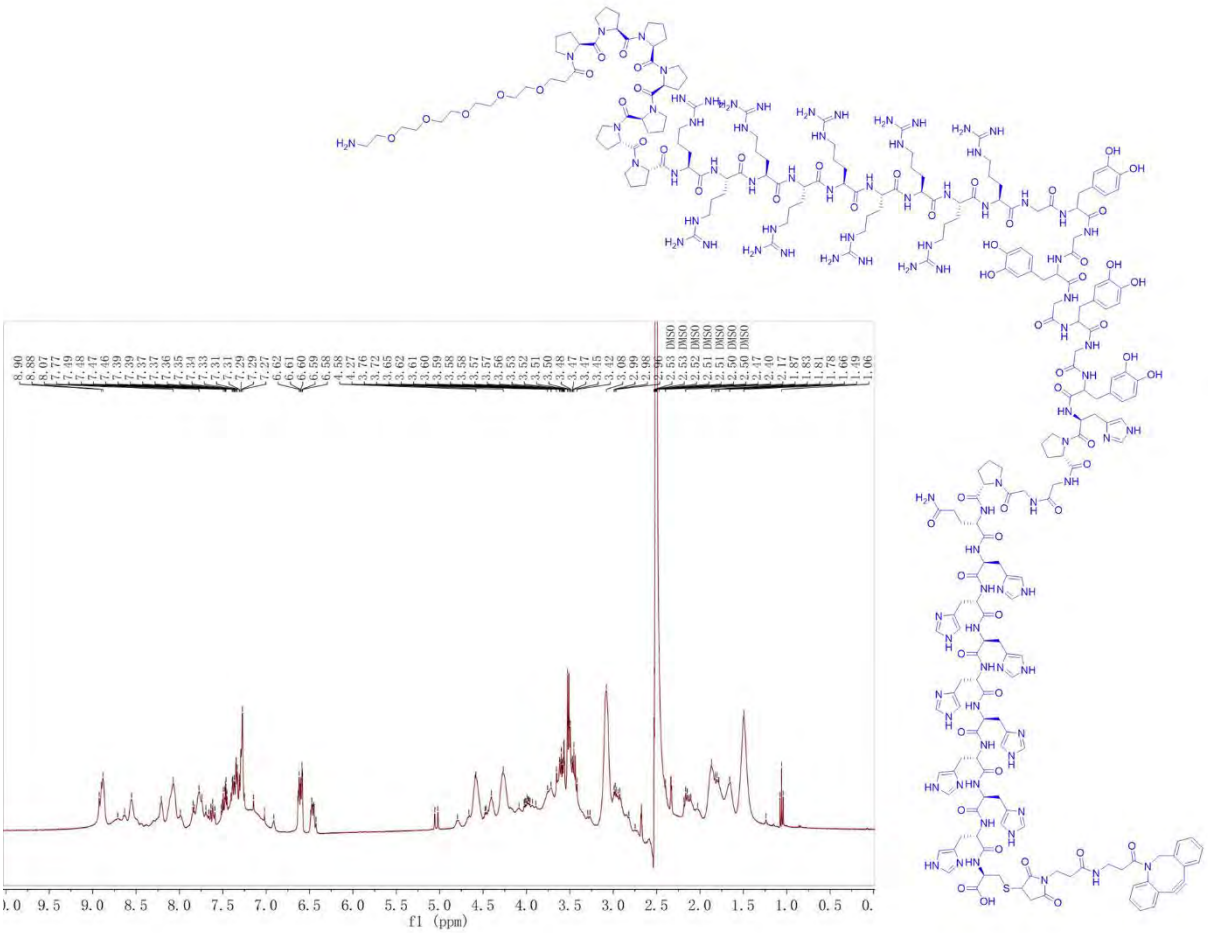


**Figure S1.** Chemical structure and $^{1}$H NMR spectrum of PEG5-P7-R9-(G-DOPA)4-HPGGPQ-H8-C-DBCO.

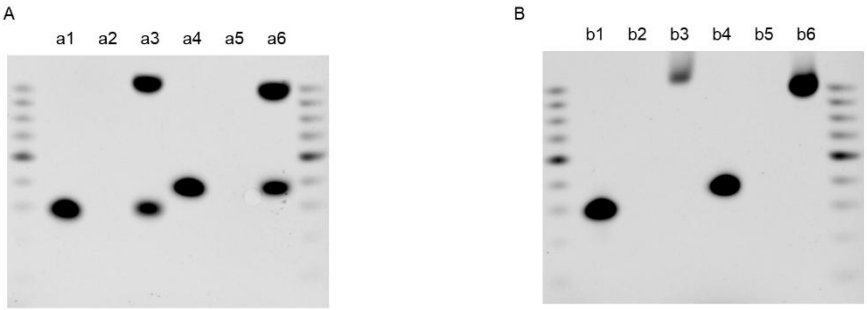


**Figure S2.** Urea-PAGE analysis of miRNA-124-Azido (a1 and b1), Peptide-DBCO (a2, a5, b2 and b5), PON nanohybrids (a3 and b3), FAM-miRNA-124-Azido (a4 and b4) and FAM-labeled PON nanohybrids (a6 and b6). Peptide-DBCO is mixed with miRNA-124-Azido and FAM-miRNA-124-Azido at a ratio of 1:2 (A) and 2:1 (B), respectively. Peptide-DBCO is not observed due to its nucleotide-free structure.

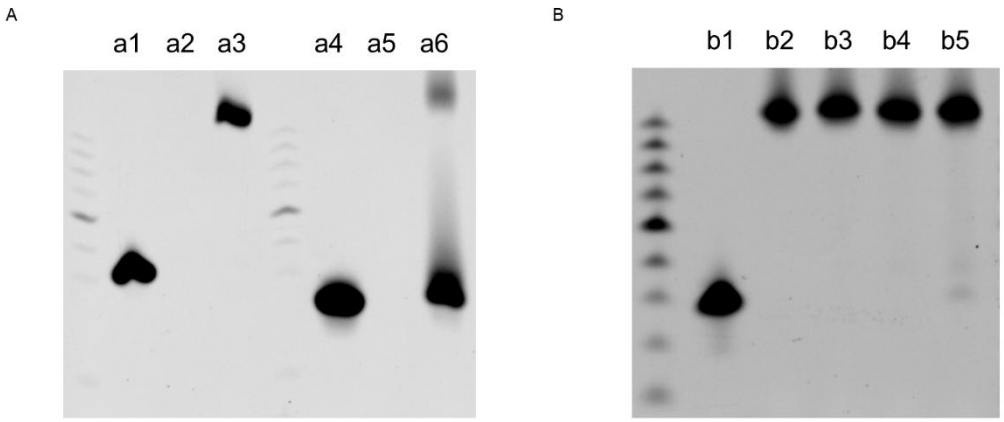


**Figure S3.** (A) Urea-PAGE analysis of miRNA-124-Azido (a1), Peptide-DBCO (a2 and a5), PON nanohybrids (a3), NC-RNA (a4) and NC-RNA+Peptide-DBCO (a6). (B) Urea-PAGE analysis of miRNA-124-Azido (b1), PON nanohybrids in 10% FBS at pH = 4.5 (b2), 5.5 (b3), 6.5 (b4), 7.5 (b5). Peptide-DBCO is not observed due to its nucleotide-free structure.

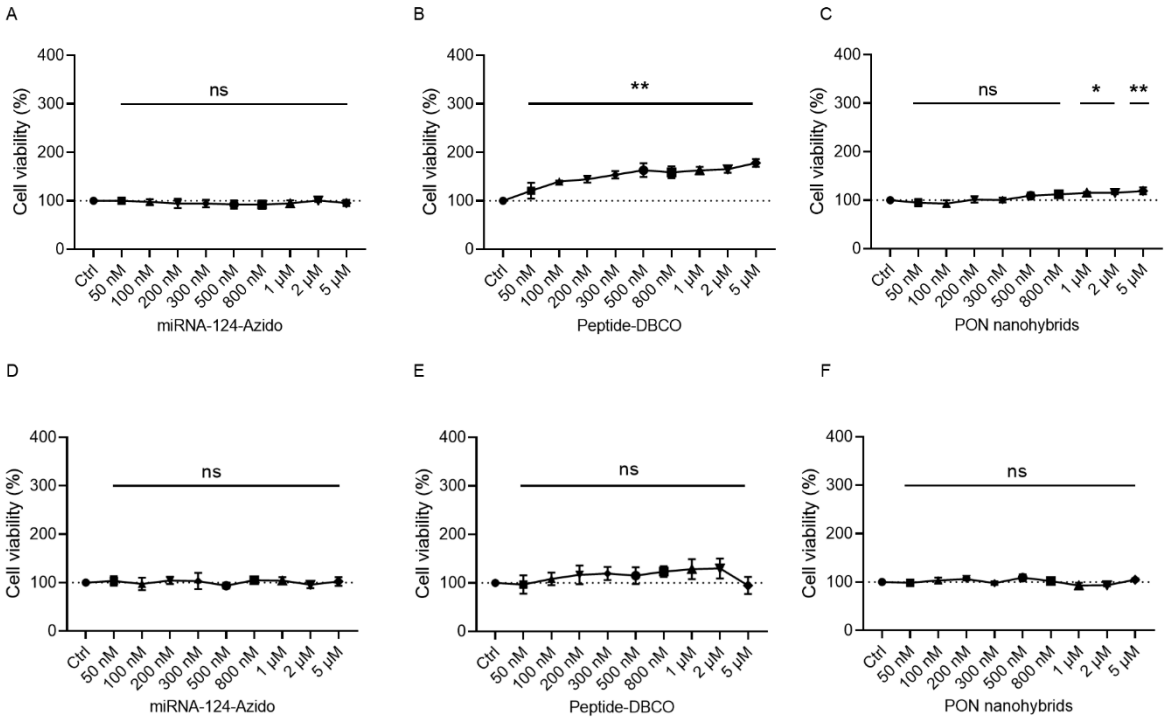


**Figure S4.** Viability of the RAW264.7 cells (A-C) and BMDMs (D-F) after incubation with miRNA-124-Azido, Peptide-DBCO, and PON nanohybrids at different concentrations. n = 3 per group. *$p < 0.05$, **$p < 0.01$, and ns: no significance, compared with the control group.

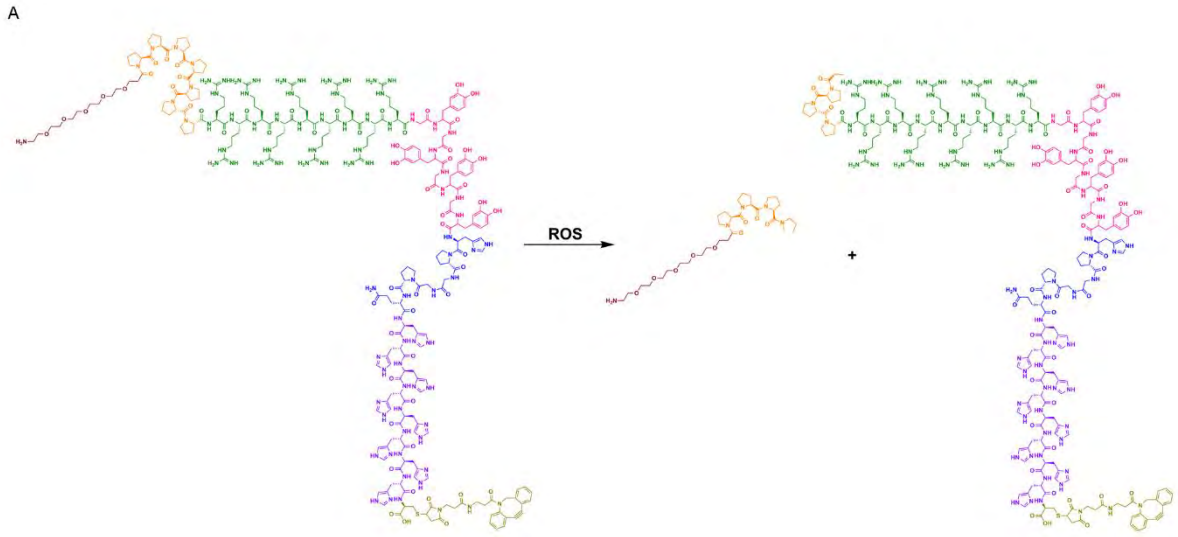


**Figure S5.** Chemical structure change of Peptide-DBCO after ROS intervention.

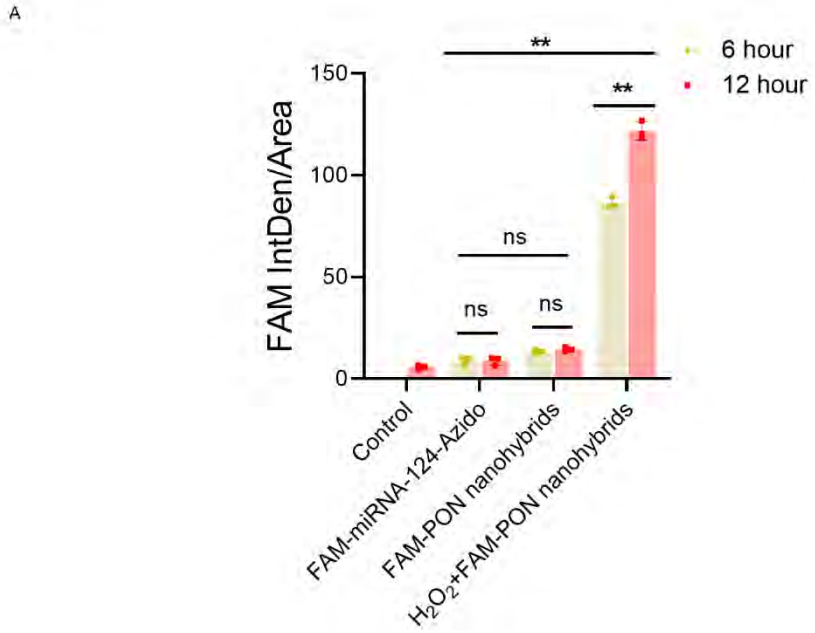


**Figure S6.** Average FAM fluorescence intensity in cells after different treatments. n = 3 per group, *$p < 0.05$, **$p < 0.01$, and ns: no significance.

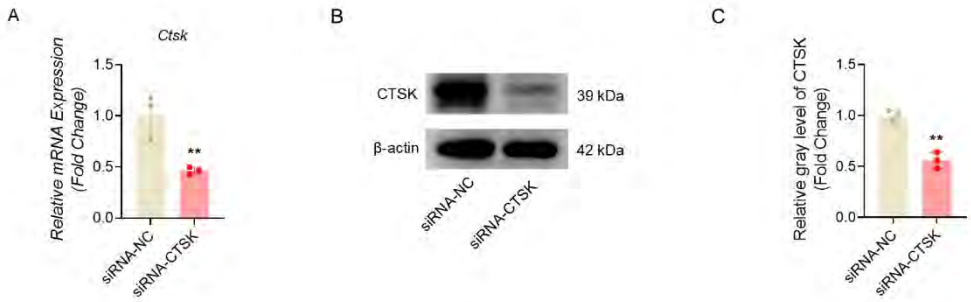


**Figure S7.** (A) mRNA level of CTSK after siRNA intervention. (B and C) Protein level of CTSK after siRNA intervention. n = 3 per group, *$p < 0.05$, **$p < 0.01$, and ns: no significance, compared with the siRNA-NC group.

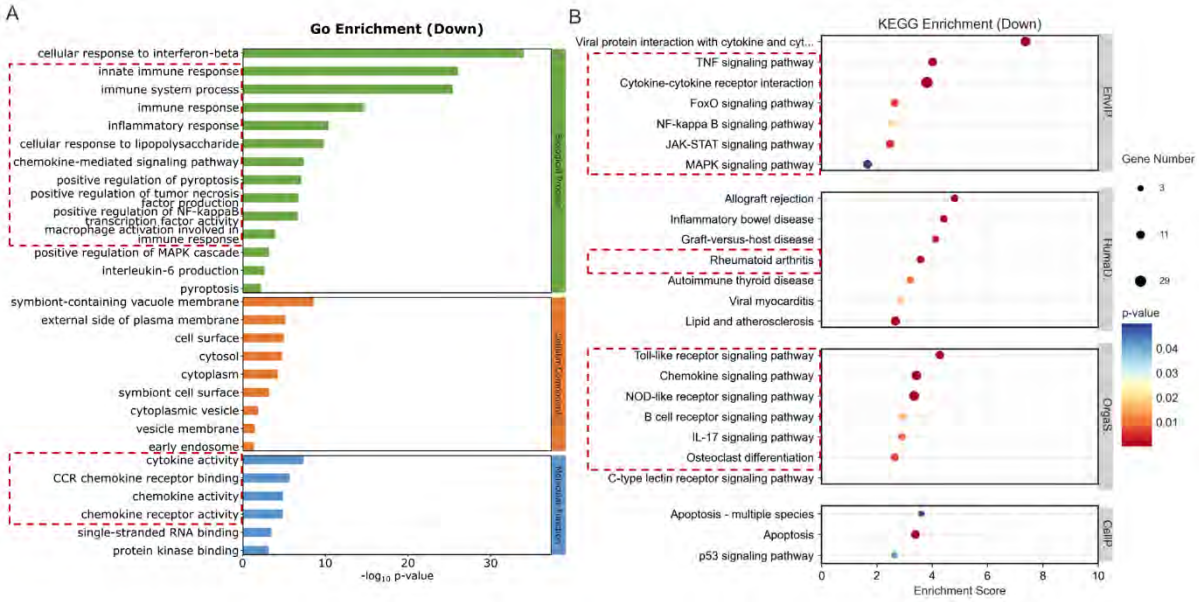


**Figure S8.** (A) Go enrichment pathway analysis of down-regulated DEGs. (B) KEGG enrichment pathway analysis of down-regulated DEGs.

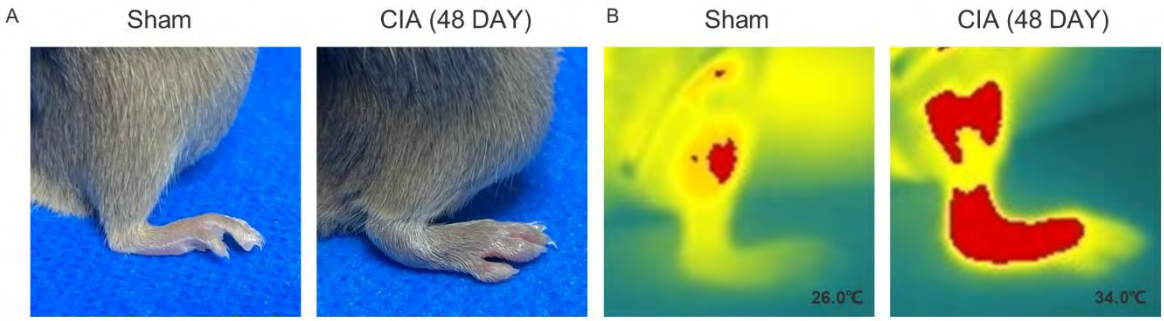


**Figure S9.** Macroscopic observations (A) and thermographic images (B) of hindpaws.


**Figure S10.** Three-dimensional micro-CT images of forepaws (A), knees (B), and hindpaws (C).

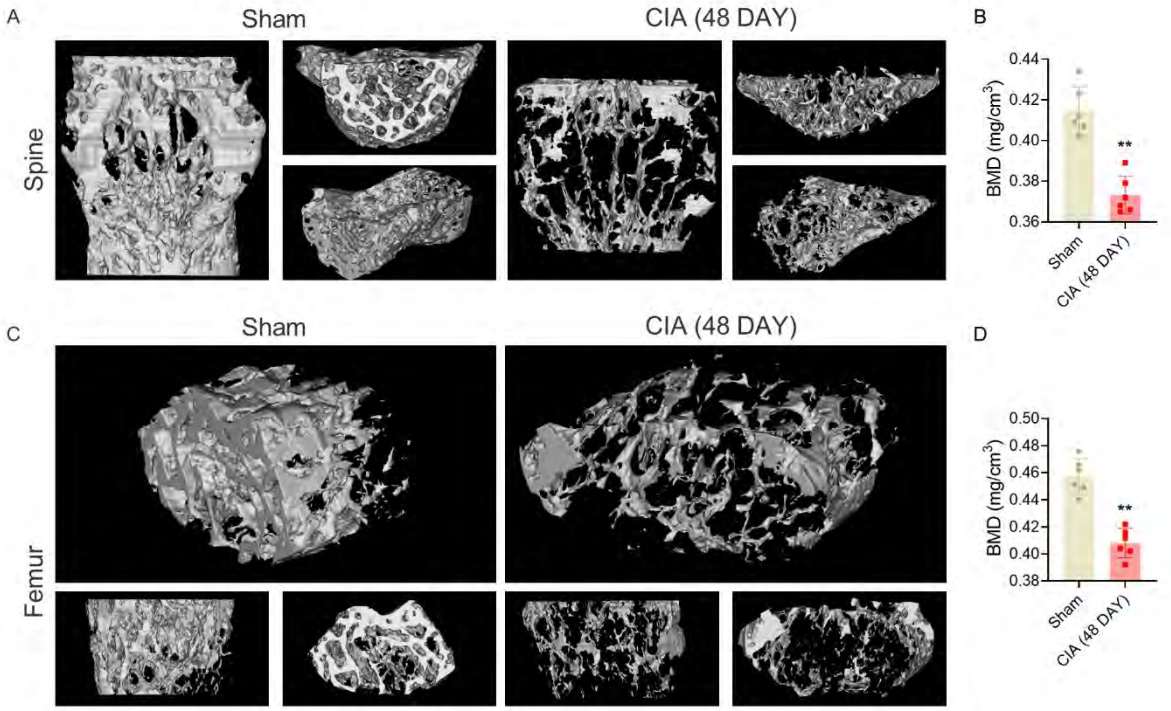


**Figure S11.** (A) Three-dimensional micro-CT images of the second lumbar (L2) vertebra. (B) Quantitative analysis of BMD in L2 vertebra. (C) Three-dimensional micro-CT images of femur. (D) Quantitative analysis of BMD in femur. n = 6 per group, *$p < 0.05$, **$p < 0.01$, and ns: no significance, compared with the Sham group.

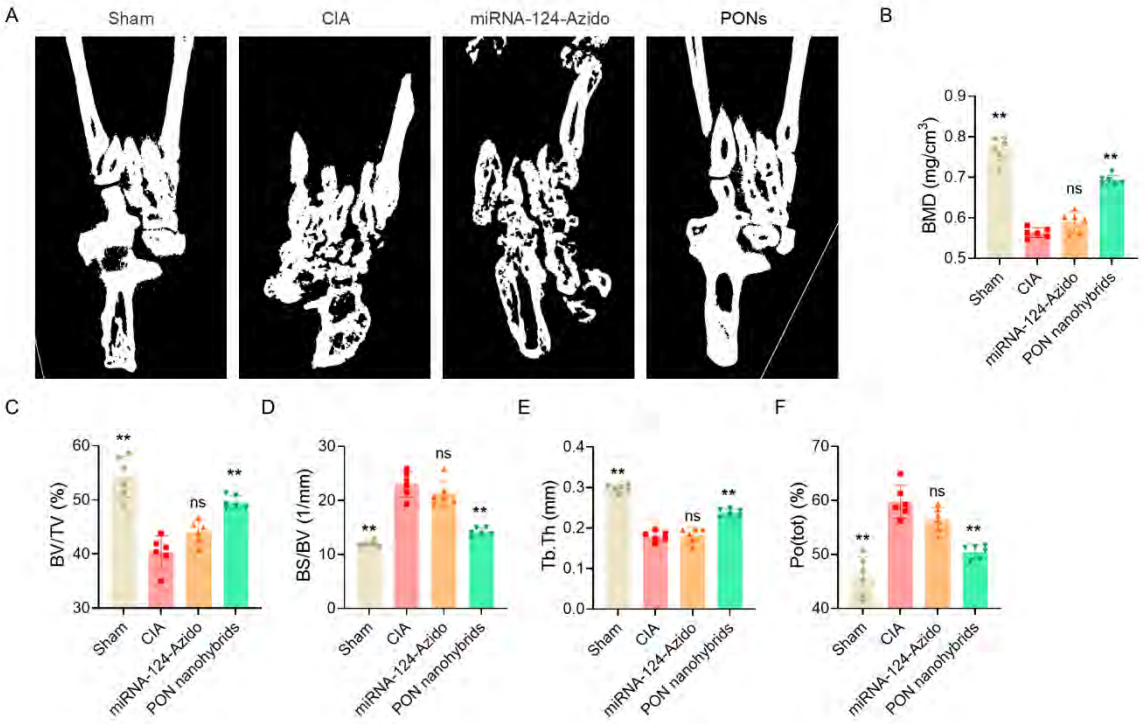


**Figure S12.** (A) Two-dimensional micro-CT images of hindpaws. (B-F) Quantitative analysis of bone morphological parameters including BMD (g/cm$^3$), BV/TV (%), BS/BV (1/mm), Tb. Th (mm), and Po tot (%). n=6 per group, *$p < 0.05$, **$p < 0.01$, and ns: no significance, compared with the CIA group.

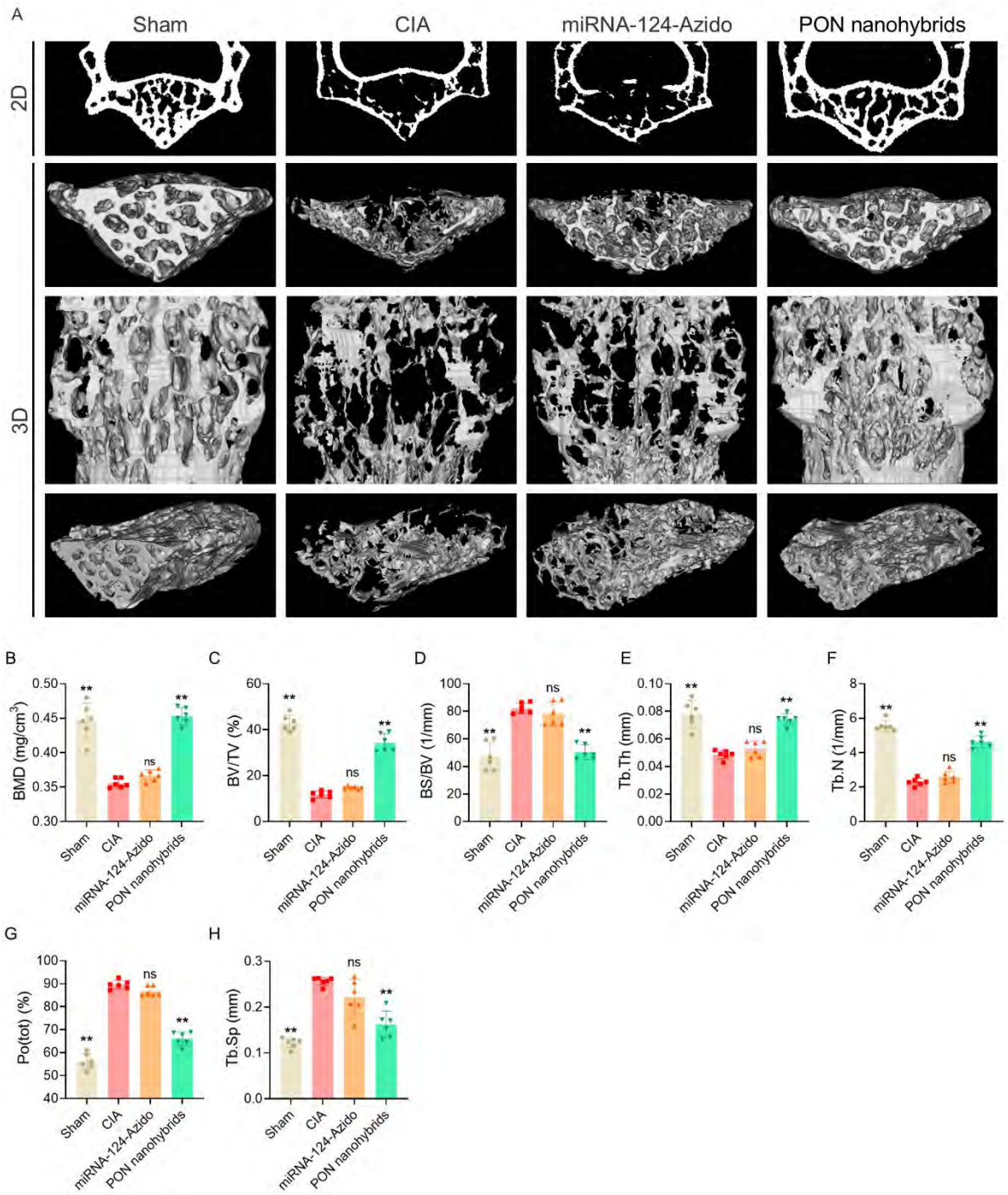


**Figure S13.** (A) Two- and three-dimensional micro-CT images of L2 vertebra. (B-H) Quantitative analysis of bone morphological parameters including BMD (g/cm$^3$), BV/TV (%), BS/BV (1/mm), Tb. Th (mm), Tb. N (1/mm), Po tot (%) and Tb. Sp (mm). n = 6 per group, *$p < 0.05$, **$p < 0.01$, and ns: no significance, compared with the CIA group.

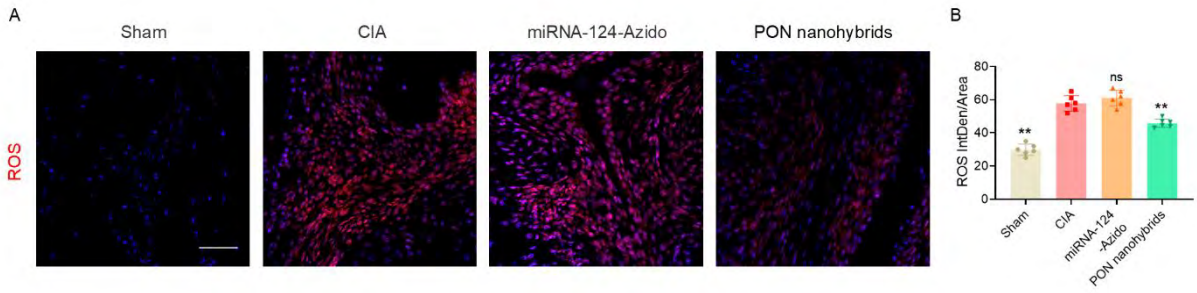


**Figure S14.** (A) DHE staining of ROS levels in knee synovial tissues (Scale bar = 200 μm). (B) Quantitative analysis of ROS fluorescence intensity in synovial tissues. n = 6 per group, $*p < 0.05$, $**p < 0.01$, and ns: no significance, compared with the CIA group.

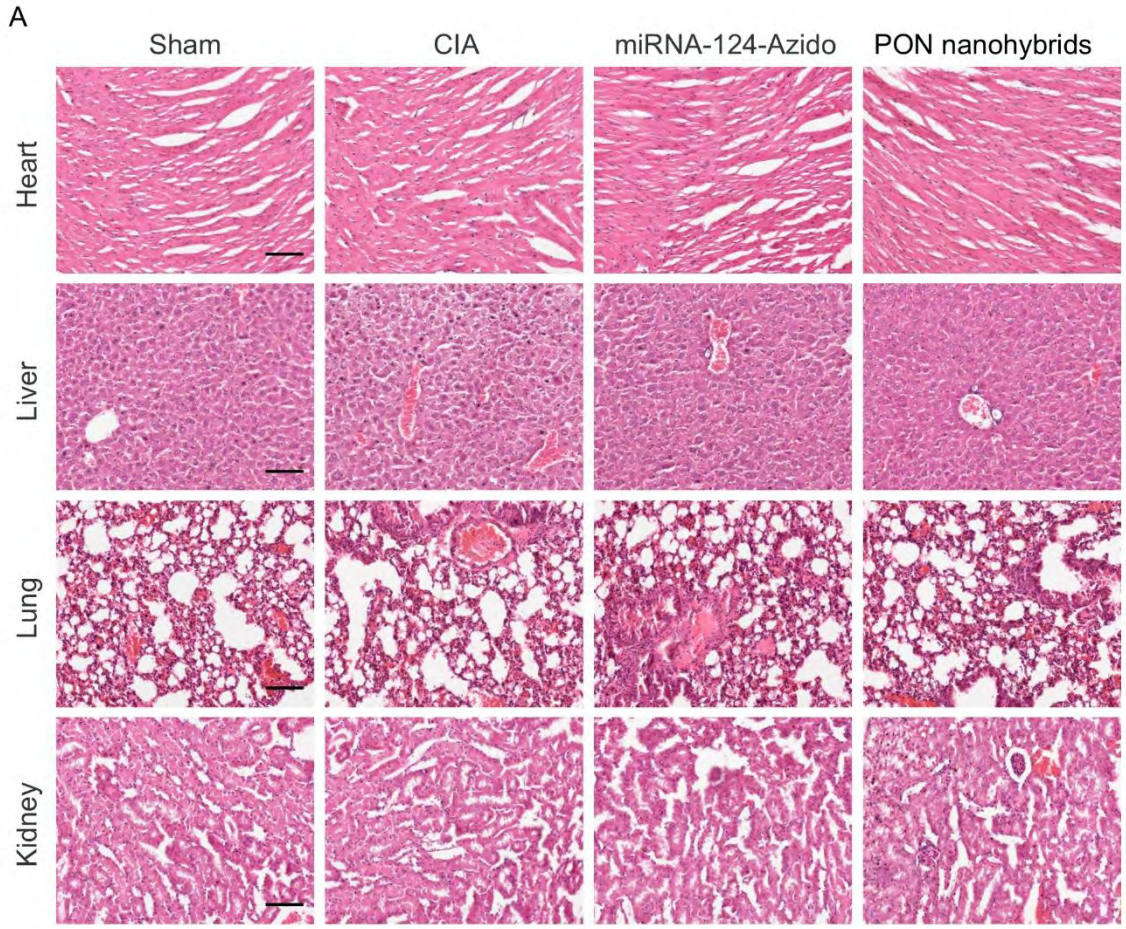


**Figure S15.** H&E staining of heart, liver, lungs, and kidneys (Scale bar = 200 μm).

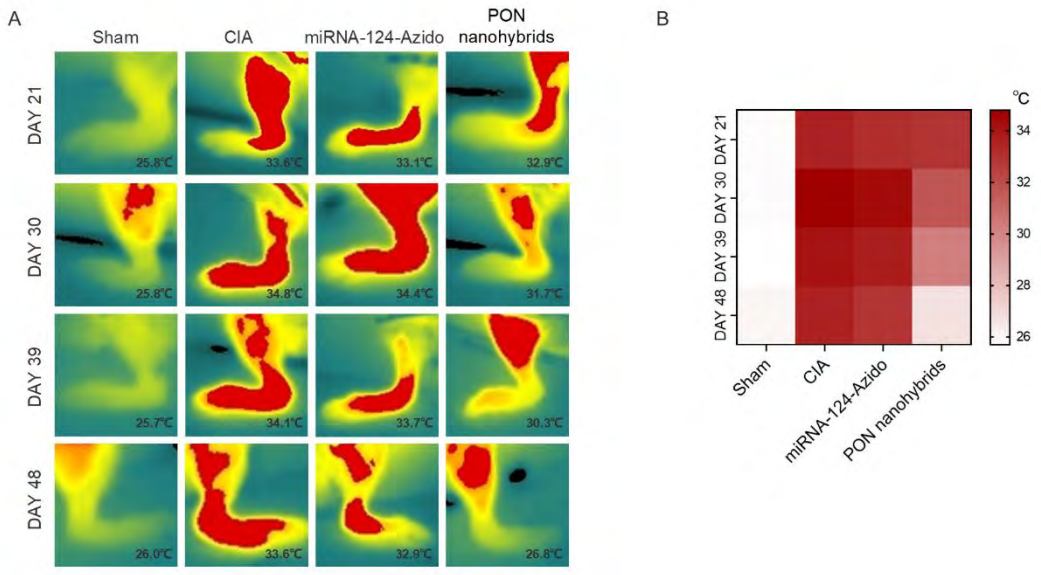


**Figure S16.** (A) Thermographic images of the hindpaws. (B) Heatmap of thermographic images.

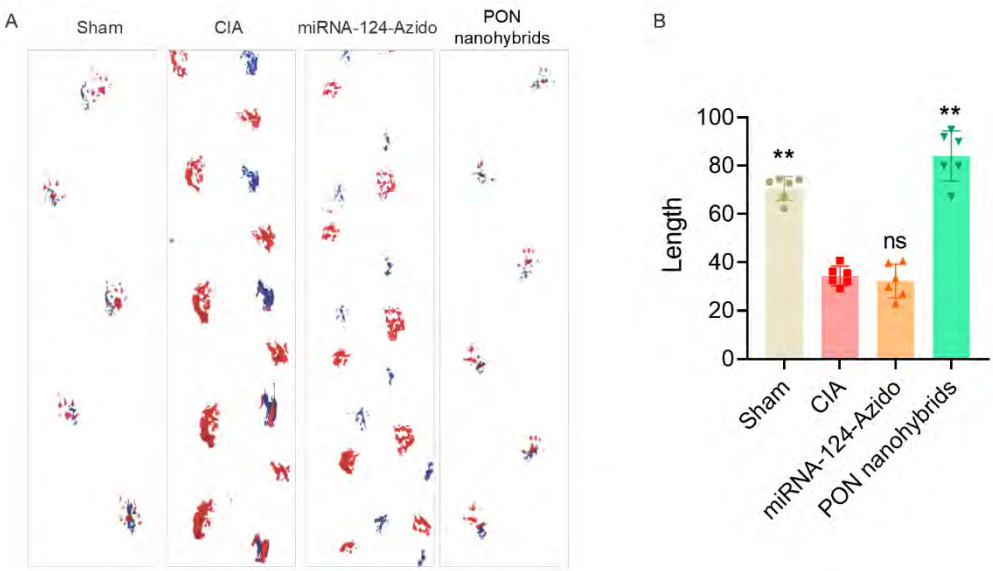


**Figure S17.** (A) Representative images of gait analysis. (B) Quantitative analysis of stride length. n = 6 per group, *$p < 0.05$, **$p < 0.01$, and ns: no significance, compared with the CIA group.

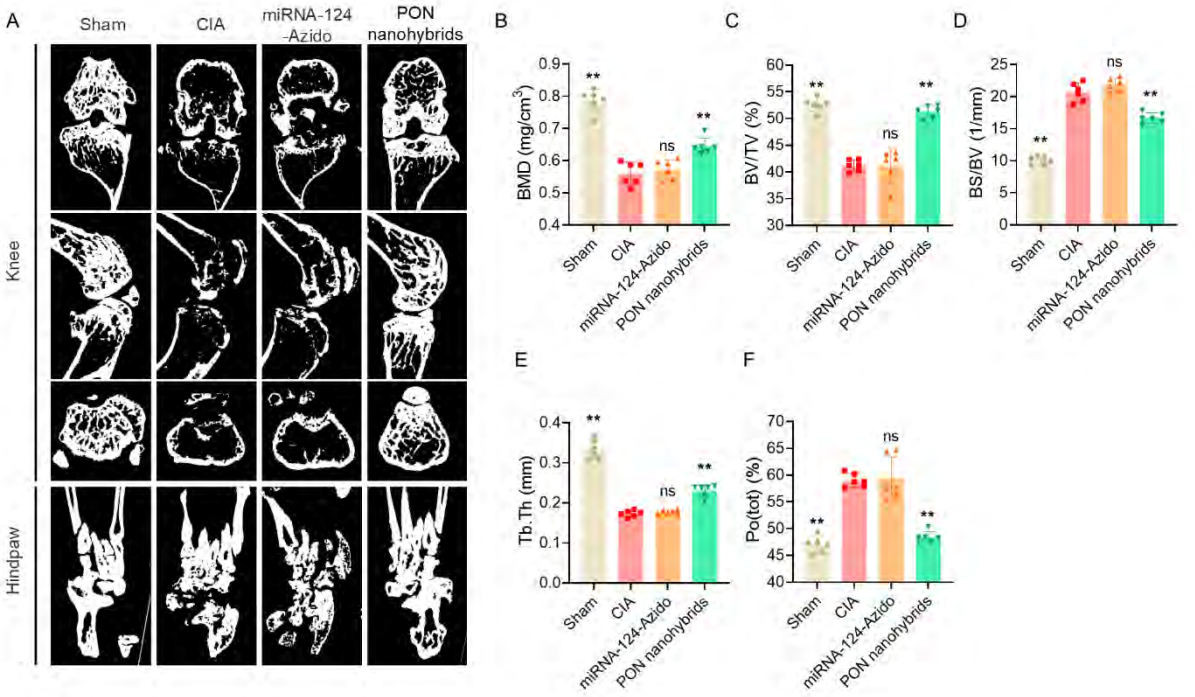


**Figure S18.** (A) Two-dimensional micro-CT images of knees and hindpaws. (B-F) Quantitative analysis of bone morphological parameters including BMD (g/cm$^3$), BV/TV (%), BS/BV (1/mm), Tb. Th (mm) and Po tot (%). n = 6 per group, *$p < 0.05$, **$p < 0.01$, and ns: no significance, compared with the CIA group.

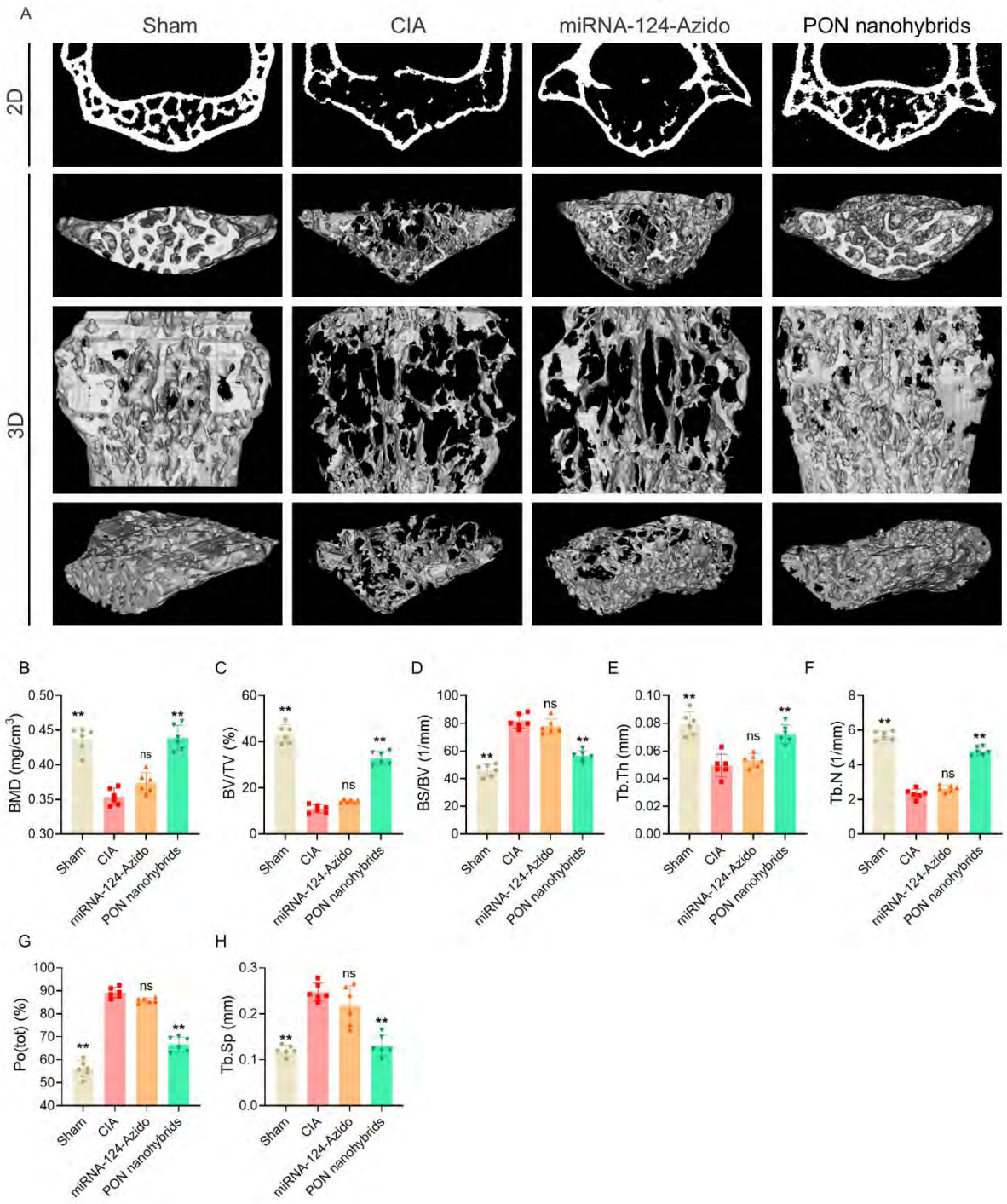


**Figure S19.** (A) Two- and three-dimensional micro-CT images of L2 vertebra. (B-H) Quantitative analysis of bone morphological parameters including BMD (g/cm$^3$), BV/TV (%), BS/BV (1/mm), Tb. Th (mm), Tb. N (1/mm), Po tot (%) and Tb. Sp (mm). n = 6 per group, *$p < 0.05$, **$p < 0.01$, and ns: no significance, compared with the CIA group.

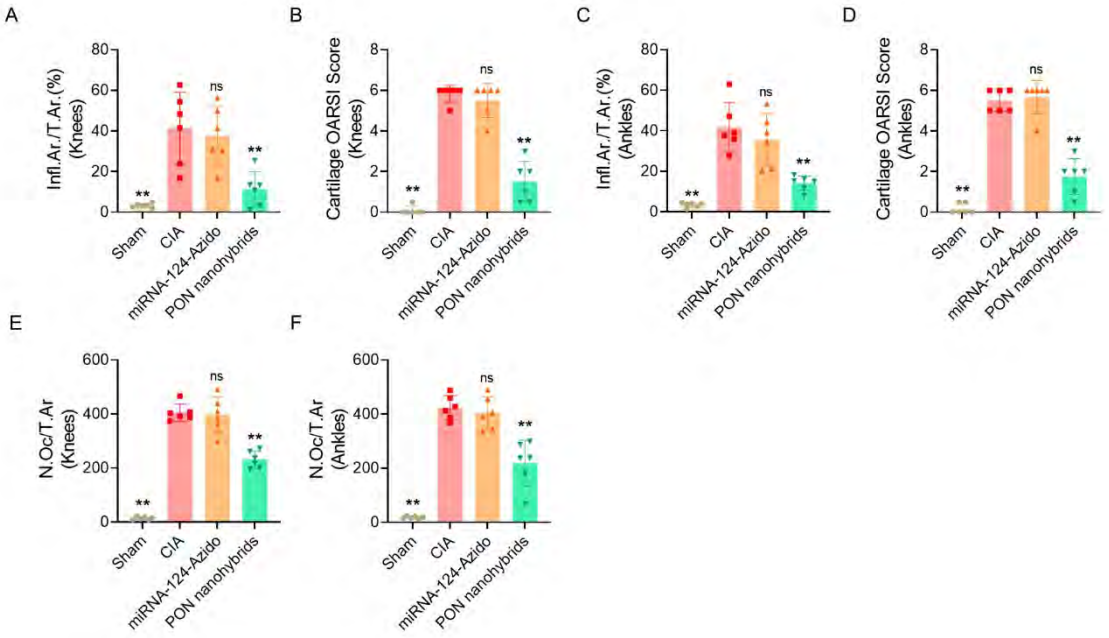


**Figure S20.** (A-D) Quantitative analysis of inflammation area per tissue area (Infl. Ar./T.Ar.) and cartilage OARSI score in knees and ankles. (E and F) Quantitative analysis of osteoclast number per tissue area (N.Oc./T.Ar.) in knees and ankles. n = 6 per group, *$p < 0.05$, **$p < 0.01$, and ns: no significance, compared with the CIA group.

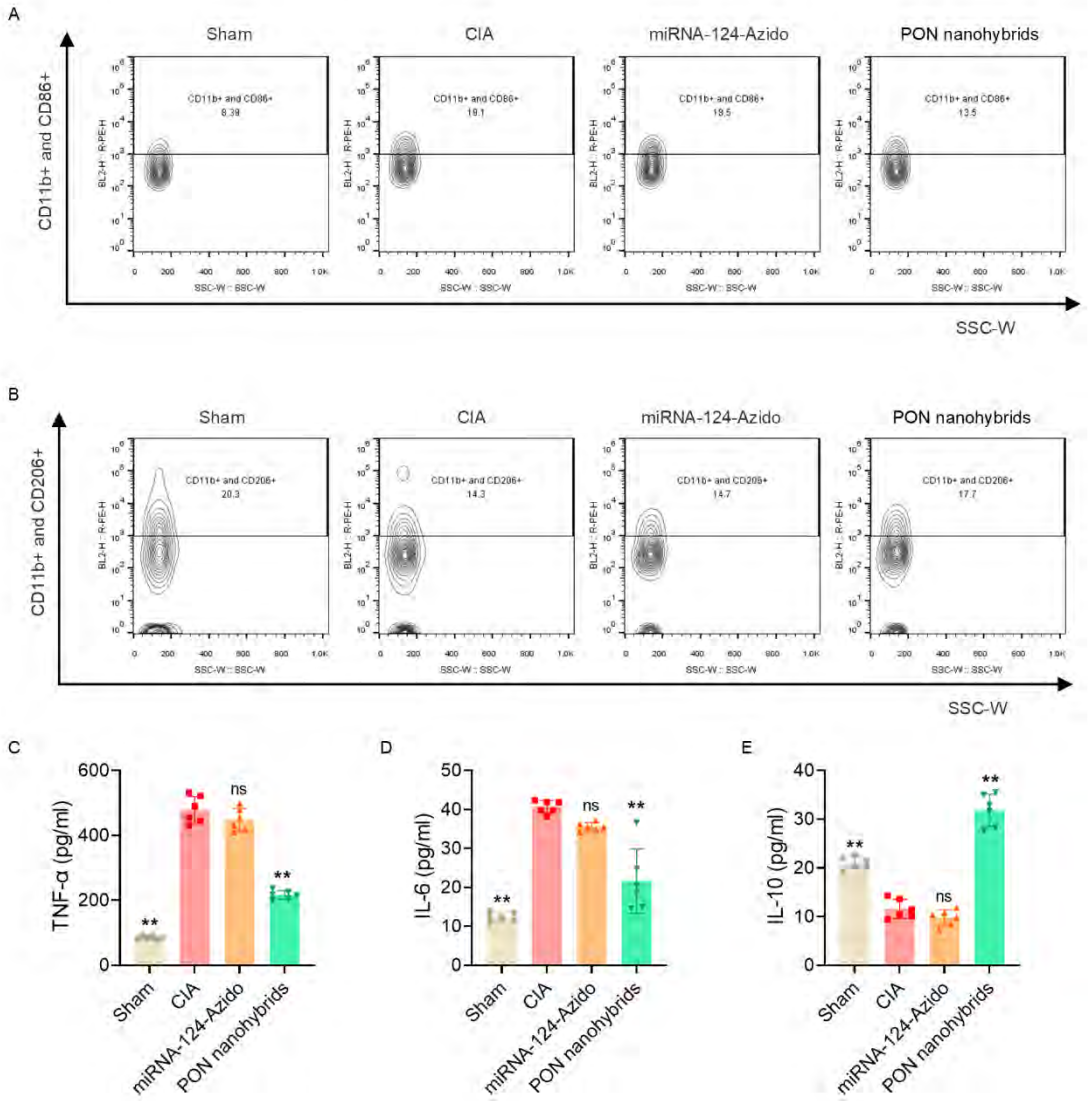


**Figure S21.** (A) Flow cytometry analysis of CD11b+/CD86+ cells in splenic tissues. (B) Flow cytometry analysis of CD11b+/CD206+ cells in splenic tissues. (C-E) ELISA analysis of TNF-α, IL-6, and IL-10 in serum. n = 6 per group, $*p < 0.05$, $**p < 0.01$, and ns: no significance, compared with the CIA group.

**Table S1.**

Primer sequences used for qRT-PCR.

| Gene (mus) | Forward Primers (5'-3') | Reverse Primers (5'-3') |
|---|---|---|
| β-actin | GTGCTATGTTGCTCTAGACTTCG | ATGCCACAGGATTCCATACC |
| iNOS | ATCTTGGAGCGAGTTGTGGATTGTC | TAGGTGAGGGCTTGGCTGAGTG |
| Arg-1 | CATATCTGCCAAAGACATCGTG | GACATCAAAGCTCAGGTGAATC |
| CD86 | ACGGAGTCAATGAAGATTTCCT | GATTCGGCTTCTTGTGACATAC |
| CD206 | CCTATGAAAATTGGGCTTACGG | CTGACAAATCCAGTTGTTGAGG |
| TNF-α | ATGTCTCAGCCTCTTCTCATTC | GCTTGTCACTCGAATTTTGAGA |
| IL-6 | CTCCCAACAGACCTGTCTATAC | CCATTGCACAACTCTTTTCTCA |
| IL-10 | TTCTTTCAAACAAAGGACCAGC | GCAACCCAAGTAACCCTTAAAG |
| Nfatc1 | GAGAATCGAGATCACCTCCTAC | TTGCAGCTAGGAAGTACGTCTT |
| Acp5 | CAAGAACTTGCGACCATTGTTA | ATCCATAGTGAAACCGCAAGTA |
| Mmp9 | CAAAGACCTGAAAACCTCCAAC | CAAAGACCTGAAAACCTCCAAC |
| Ctsk | GCTTGGCATCTTTCCAGTTTTA | CAACACTGCATGGTTCACATTA |
| Atp6v0a3 | GGACCATATCCCTTTGGCATT | AAAGCTCAGGTGGTTCGTGG |

**Movies S1**. miRNA-124-Azido (miRNA-124-A5-$(CH_2)$6-Azido) and Peptide-DBCO (PEG5-P7-R9-(G-DOPA)4-HPGGPQ-H8-C-DBCO) are dissolved in Diethylpyrocarbonate (DEPC) water and then mixed at 1:1 ratio. The complex self-assembles into nanoparticles through amphiphilic electrostatic interactions, a process evidenced by the solution transitioning from a transparent to a homogeneous turbid state.